

Research Paper

Numerical simulation of environmental and seismic loading of 10 MW monopile offshore wind turbines in liquefiable seabed

Tianju Wang^{a,b}, Degao Zou^{a,b,*}, Jingmao Liu^{a,b}, Kai Chen^{a,b}, Xiuyang Zhang^{a,b}, Guoyang Yi^{a,b}

^a The State Key Laboratory of Coastal and Offshore Engineering, Dalian University of Technology, Dalian, Liaoning 116024, China

^b School of Infrastructure Engineering, Dalian University of Technology, Dalian, Liaoning 116024, China

ARTICLE INFO

Keywords:

3D SBFEM-FEM

State-dependent constitutive

10 MW OWT

Liquefaction

Seismic

Deformation Mode

ABSTRACT

With the gradual application of 10 MW offshore wind turbines (OWTs) in the world, it is very important to study the liquefaction response of high power OWTs under multiple fields. In this paper, based on the state-dependent generalized plasticity model, a cross-scale refined analysis model of structure-monopile-liquefied seabed is established, and a method for the analysis of seismic dynamic response of large-diameter monopile offshore wind turbine (MOWT) in liquefiable seabed is developed. The applicability of the proposed method is validated through simulations of existing centrifuge model tests. Using this approach, the dynamic response characteristics of a 10 MW MOWT under combined wind, wave, and seismic loading are systematically investigated. The study reveals the spatial distribution of seabed liquefaction under varying earthquake intensities, elucidates the flow mechanisms, and explores the effects of different loading conditions and relative depth (R_d) of liquefiable sandy soil on the system's response. The results show that: 1. Seismic loads significantly influence seabed liquefaction, while environmental loads primarily cause cumulative rotation in MOWT. 2. As R_d increases, the rate of pore pressure accumulation slows, and liquefaction depth, soil strain around the pile, MOWT deflection, and rotation angle all increase. 3. Liquefaction results in overall subsidence of the soil within a range of one pile diameter ($1D$, $D = 10.375$ m) around the pile, while soil flow and heave within a range of $2D$ behind the pile are the main contributors to foundation rotational failure.

1. Introduction

Offshore wind power, as a new type of clean energy, is an important part of the global response to climate change, the energy transition and achieving carbon neutrality. In recent years, offshore wind power has been growing rapidly around the world, as shown in Fig. 1. The Global Wind Energy Council (GWEC) projects that the compound annual growth rate (CAGR) of offshore wind energy will reach 28 % over the next five years (GWEC, 2024). From 2024 to 2028, the global installed capacity of offshore wind is expected to increase by 138 GW. For offshore wind turbines (OWTs), especially in shallow water depths below 30 m, the support base of the OWTs can account for up to 30 % of the total construction cost of a typical offshore wind project. (Wu et al., 2019), and 12–25 % life-cycle costs ((Musial and Ram, 2010; Versteijlen et al., 2011)). Due to the special characteristics of the marine environment, offshore wind power support foundations are subjected to a variety of loads from waves, currents, wind, 1P (rotor frequency), 3P

(frequency induced by blade passage past the tower), earthquakes, etc., which generate large overturning moments and vibrations on the foundations, and therefore the design and stability of the pile foundations are crucial for the safe operation of OWTs.

The application of high power OWTs has become a growing trend, with Europe planning to market the largest OWT in 2024, with a prototype having an impeller diameter of 236 m and a power rating of 15 MW (Vestas, 2022), and China already having successfully grid-connected and operated the largest OWT in 2023 (GWH252-16 MW), with an impeller diameter of 252 m and a rated power of 16 MW (Goldwind, 2023). As of now, OWTs with a capacity of 10 MW and above account for 17.2 % of the total installed capacity in China. In the future, newly installed turbines will primarily be 8.5 MW or larger. For instance, the Xu Wen offshore wind farm in China has installed 25 units of 12 MW monopile offshore wind turbines (MOWT), which successfully achieved full-capacity grid connection by the end of 2024. Most of the current studies on large diameter MOWT focus on the horizontal cyclic

* Corresponding author.

E-mail address: zoudegao@dlut.edu.cn (D. Zou).

<https://doi.org/10.1016/j.compgeo.2025.107358>

Received 17 January 2025; Received in revised form 14 May 2025; Accepted 15 May 2025

Available online 22 May 2025

0266-352X/© 2025 Elsevier Ltd. All rights reserved, including those for text and data mining, AI training, and similar technologies.

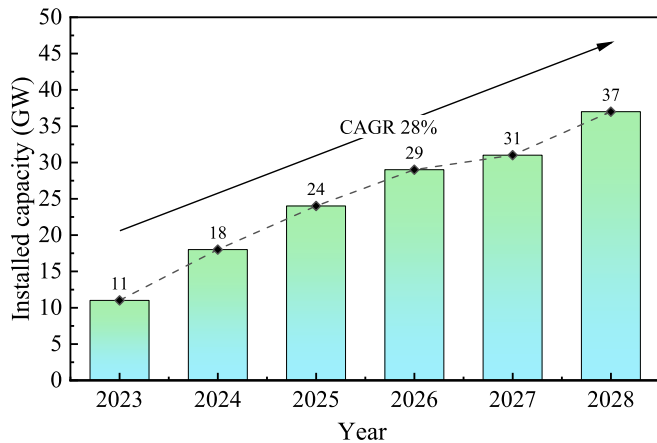


Fig. 1. Offshore wind new installations outlook 2023–2028 (Global Wind Report, 2024).

Table 1

The numerical simulation method of MOWTs.

Researcher	PSI-research method	Installed capacity	Pile-element type	Research method
Yang et al., 2020	p-y spring elements	10 MW	Beam	BNWF
Yan et al., 2021	p-y and q-z spring elements	10 MW	shell	BNWF
Patra and Haldar, 2021	p-y, t-z, and q-z spring elements	10 MW	beam	BNWF
Shi et al., 2022	p-y, t-z, and q-z spring elements	5 MW	beam	BNWF
Zhang et al. (2022a,b)	rigid beam-column link	10 MW	beam	PDMY FEM
He and Ye, 2023	interface elements	1.5 MW	solid	PZ- III FEM
Wang et al., 2023a	rigid beam-column link	3 MW	beam	PDMY FEM
Sahraeian et al., 2023	rigid beam-column link	5 MW	beam	PDMY FEM
This study	Saturated porous interface elements	10 MW	solid	PZ-DUT SBFEM-FEM

response and seismic dynamic response with a capacity of 3–5 MW (Kim et al., 2014; Santangelo et al., 2016; Zuo et al., 2018; Cheng et al., 2021; Mo et al., 2021; Patra and Haldar, 2021; Patra et al., 2022; Eslami and Ghorbani, 2022; Sun et al., 2022; Cheng et al., 2024), and there are relatively few studies on the pile-soil interaction and the dynamic response characteristics of the structure of a 10 MW OWT under the multiple fields, so there is an urgent need for the study of the

liquefaction response of 10 MW OWT systems in saturated sandy soils under the action of multiple loads, such as wind, wave, and seismic loads.

Several researchers have investigated the dynamic response of OWTs to factors such as wind load, wave load, and seismic load. These studies typically focus more on the response of the upper structure, neglecting the more significant pile-soil interaction (PSI) effects under seismic loading (Jonkman and Buhl, 2005; Prowell et al., 2010; Asareh and Prowell, 2011; Santangelo et al., 2016; Asareh et al., 2016). For the lower single-pile foundation, Cui et al. (2023) obtained the corresponding analytical solution by combining the potential function method and the method of separation of variables, investigating the influence of radial soil heterogeneity on the horizontal vibration characteristics of piles in saturated soil. Wang et al. (2024) proposed an analytical solution for the horizontal vibration of partially embedded offshore piles, considering the effect of wave load distribution. They explored how wave load distribution affects the horizontal vibration of partially embedded offshore piles.

PSI significantly affects the dynamic response and natural frequency of OWTs. In existing research, numerical simulations of the seismic response of MOWTs typically employ the nonlinear Winkler model, which considers pile-soil dynamic interaction through springs (p -y, t -z, and q -z) and dampers. (Liyanapathirana and Poulos, 2005; Zhao and Maissner, 2006; Brandenburg Scott et al., 2013; Kim et al., 2014; Sapountzakis et al., 2015; Janalizadeh and Zahmatkesh, 2015; Wang et al., 2018; Ju and Huang, 2019; Yang et al., 2020; Xi et al., 2021; Yan et al., 2021; Patra and Haldar, 2021; Shi et al., 2022). Cheng et al. (2022) developed a novel cyclic p -y elastoplastic model based on the bounding surface theory, which can well capture the main characteristics of pile-head load–displacement curve, such as nonlinearity, hysteresis, displacement accumulation, and stiffness degradation. However, the p -y curve method in existing standards (American Petroleum Institute (API), 2011; Det Norske Veritas (DNV), 2013) is based on data from small-diameter piles subjected to fewer than 100 cycles of testing, and it does not account for the effects of large diameter and high-frequency radiation damping. Therefore, for large-diameter structures, a comprehensive finite element model of the soil domain is required (Massah-Fard et al., 2024).

Some studies have analyzed the liquefaction response of fixed foundations for offshore wind turbines using advanced constitutive models. They have employed advanced elastoplastic constitutive models such as the generalized plasticity model (Cuéllar et al., 2012b), the Tsinghua sand liquefaction plasticity model (Wang et al., 2016), the SANISAND model (Liu and Kaynia, 2022), and the PDMY02 (Abbasi et al., 2023) to discuss the dynamic response of pile foundations in liquefied sand under the influence of factors such as cyclic lateral loading, pile caps, non-liquefiable surface layers, geometric shapes, vertical loads, and bidirectional loading. However, the aforementioned methods involve complex hardening rules and a large number of elements, resulting in relatively low computational efficiency when

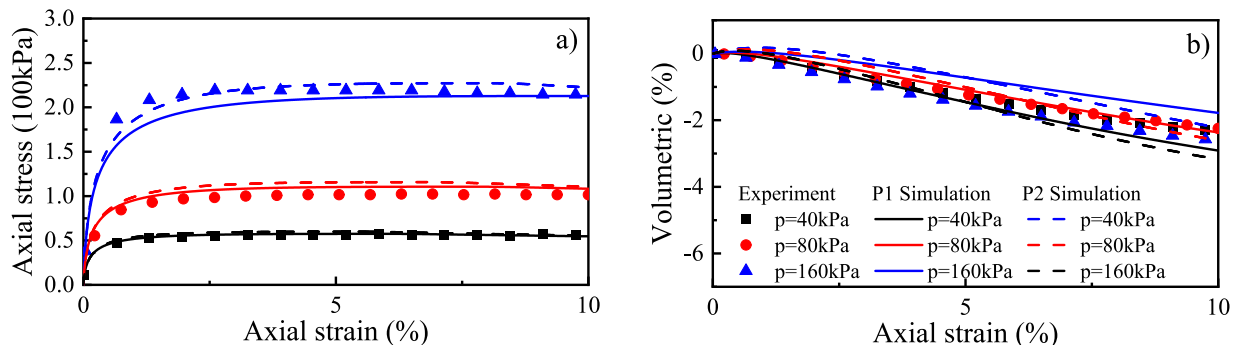


Fig. 2. Simulation of triaxial drained constant p tests for Nevada sandy soil with $Dr = 40\%$.

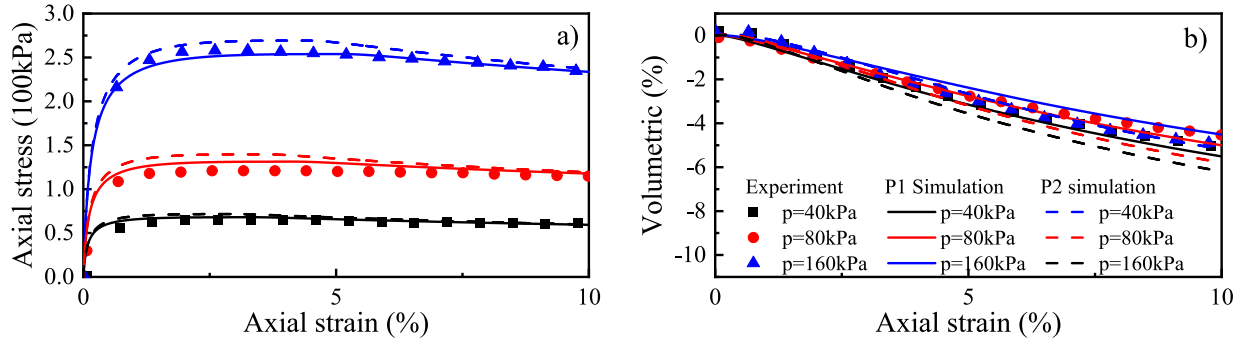


Fig. 3. Simulation of triaxial drained constant p tests for Nevada sandy soil with $Dr = 60\%$.

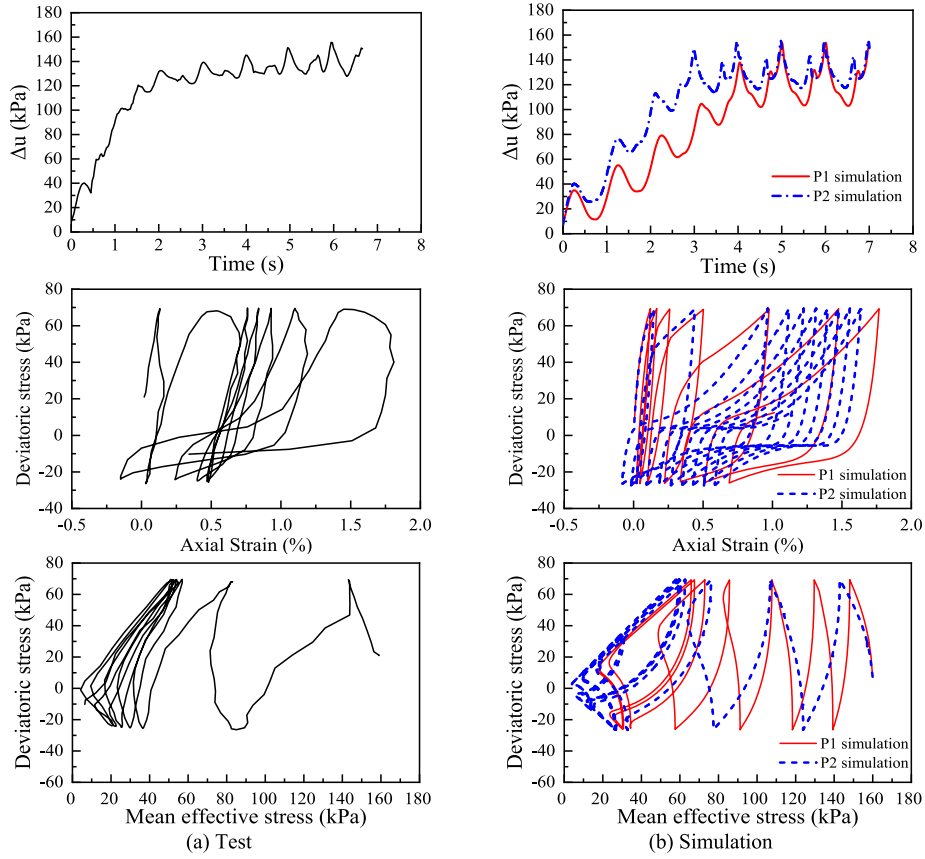


Fig. 4. Simulation in undrained cyclic triaxial tests on Nevada sand with $Dr = 40\%$.

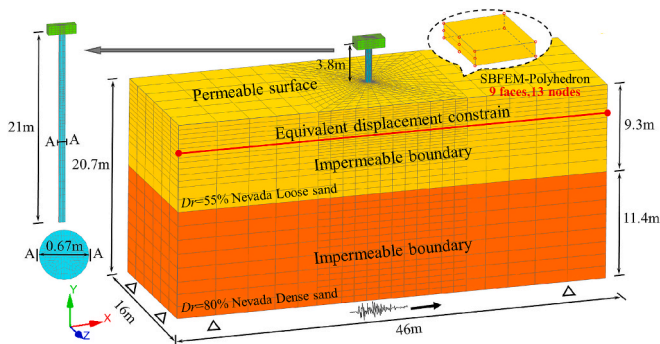
employed on standard personal computers by researchers or engineers, making them unsuitable for practical engineering applications. Table 1 summarizes methods for current MOWT numerical simulations.

In view of the above problems, there is an urgent need for a refined analysis method that can efficiently analyze the dynamic response of MOWTs in liquefied seabeds. In this study, numerical simulations are conducted using GEODYNA (Zou et al., 2022), a software that has been

extensively applied in geotechnical engineering analyses involving nuclear power plants, breakwaters, earth-rock dams, and offshore wind turbines (Zou et al., 2013; Gong et al., 2021; Qu et al., 2021; Nie et al., 2022; Chen et al., 2023; Liu et al., 2023; Zhang et al., 2024; Zhang et al., 2025). A multiscale refined numerical model is established based on the state-dependent generalized plasticity constitutive model (PZ-DUT) and the coupled Scaled Boundary Finite Element Method-Finite Element

Table 2
Simulation parameters for Nevada sand.

	Elasticity			Critical state			State dependent parameter				Dilatancy drij- mechanics		Dilatancy dp'- mechanics				
	G_0	ν	Em	Mc	λ	e_{i0}	β	n_g	n_b	α_1	r_l	h_2	m_p	h_3	α_2	α_3	c_0
P 1	150	0.1	0.5	1.14	0.022	0.809	0.4	2.5	4.5	1.0	1.0	10	0.5	10	1.5	0.1	0.5
P 2	150	0.1	0.5	1.14	0.022	0.809	0.4	2.5	4.5	0.6	1.0	10	0.5	10	1.5	1.0	0.5

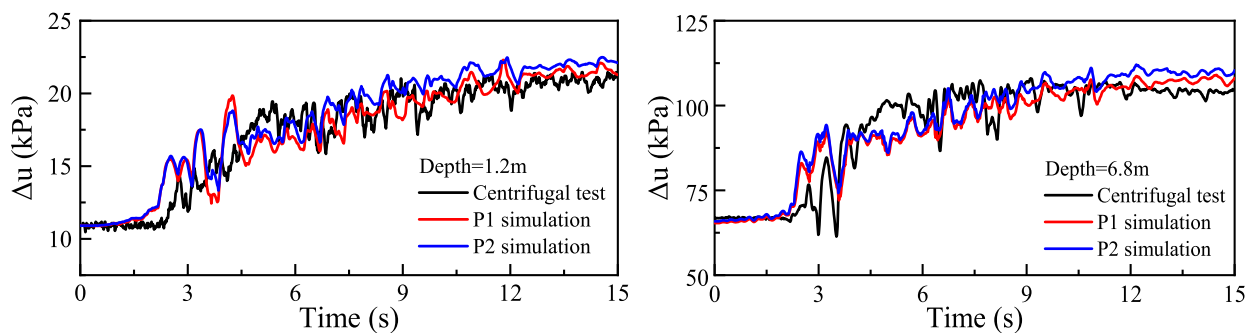


Method (SBFEM-FEM) for saturated porous media (Zou et al., 2019). A method for analyzing the seismic dynamic response of MOWT in sandy soils was developed and validated by comparing the results of centrifugal tests. A systematic study of the dynamic response characteristics of 10 MW MOWT structures under environmental and seismic loads and the pore pressure distribution law; the damage mechanism of monopile foundations in liquefiable soil layers is revealed.

In this section, a time-domain numerical method based on a state-dependent generalized plastic model is presented. Firstly, the parameters of the sandy soil constitutive model are calibrated through a simulated triaxial test. Subsequently, a three-dimensional (3D) numerical model is developed and its results are compared with those of a centrifugal test on a monopile foundation to verify the applicability of the proposed method. In addition, the influence of constitutive parameters on both element-level behavior and full-scale modeling was evaluated.

In this study, the state-dependent generalized plastic constitutive model (PZ-DUT) proposed by [Liu et al. \(2020\)](#) is used to simulate the nonlinear constitutive relationship of soil. The model is based on the framework of [Wang et al. \(1990\)](#) and [Li \(2002\)](#). The model incorporates the critical state theory of [Bardet \(1996\)](#), enabling the simulation of changes in soil physical properties under varying initial density conditions with a unified set of parameters. Three-dimensional historical memory parameters, derived from proportional memory theory, are established to accurately simulate the actual irregular earthquake loading process. Additionally, the model integrates the benefits of boundary surface theory, enhancing the simulation and applicability of soil pore ratio correlation and stress historical correlation. For the specific model framework and implementation, refer to [Liu et al. \(2018\)](#); [Liu et al. \(2020\)](#).

The above model was used to calibrate the model parameters of Nevada No 120 sands, which is the special sand of Earth Technology Corporation in VELACS project. The tests were conducted with average initial perimeter pressures ranging from 40 kPa to 160 kPa, while the relative densities of the prepared sandy soils varied between 40 percent and 60 percent, as elaborated by [Arulmoli et al. \(1992\)](#). Several constitutive models, such as PM4Sand, NTUA-Sand, and SANISAND,



4

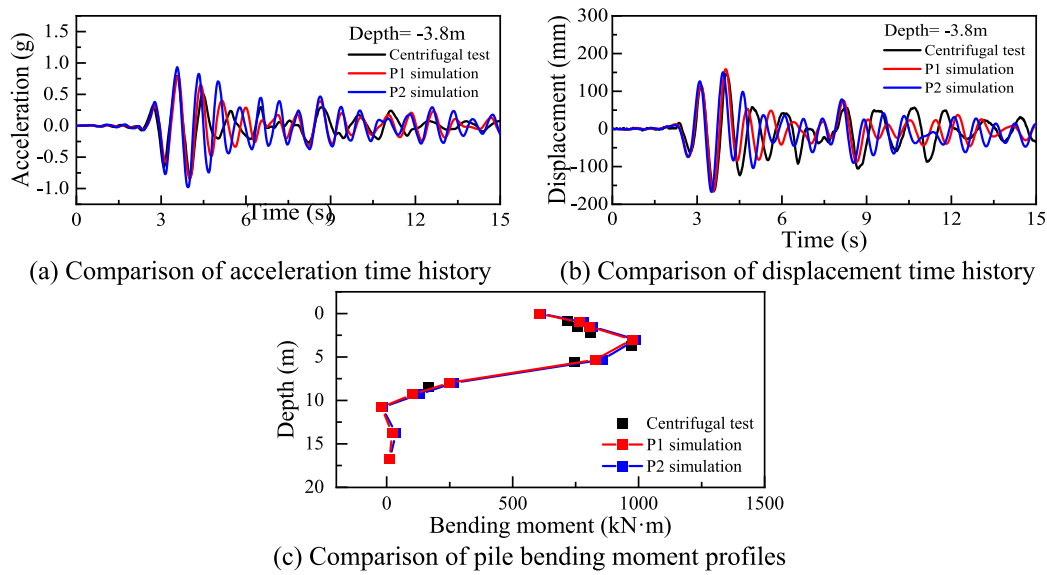


Fig. 9. Comparison of dynamic response results of superstructure and pile.

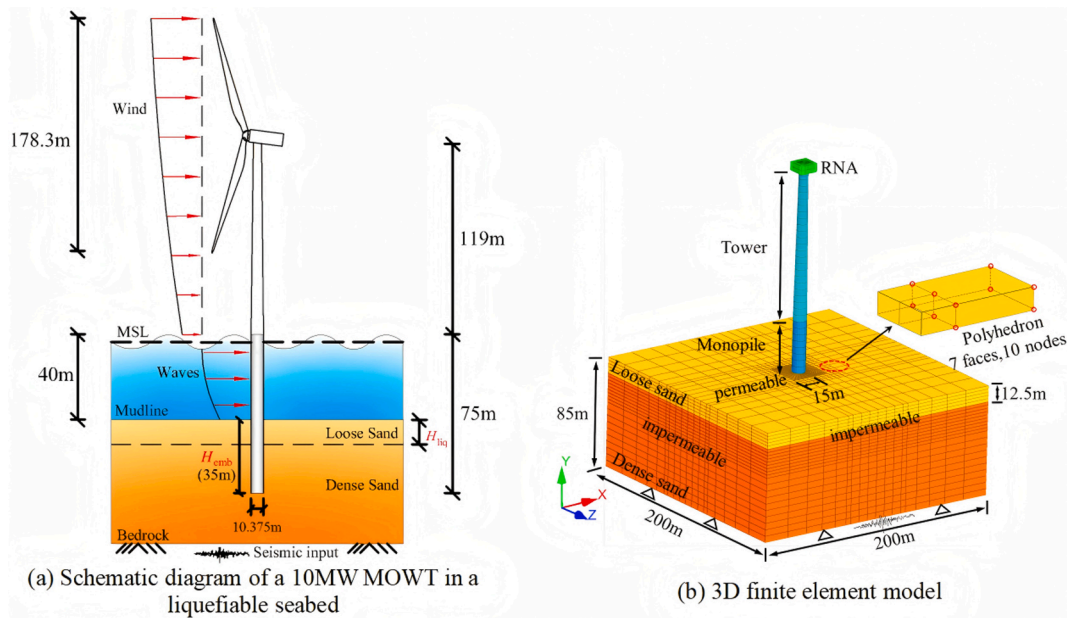


Fig. 10. Numerical model of a monopile foundation for MOWT in sands.

Table 3
Interface parameters between steel and sand.

Elasticity		Critical state			Particle crushing			Plastic modulus			Plastic flow		Loading direction	
D_{50}/kPa	D_{n0}/kPa	M_c	λ	e_{c0}	$a/\text{kPa}^{0.5}$	b	c	k	H_0/kPa	F_h	α_2	r_d	k_m	M_f
300	400	0.404	0.61	0.03	224	0.06	3.0	0.1	1500	2.5	2.5	1.0	-0.1	0.65

have been successfully calibrated against the VELACS results and other undrained cyclic tests (Boulangier and Ziotopoulou, 2015; Papadimitriou and Bouckovalas, 2002; Shahir et al., 2012).

In Figs. 2 and 3, the monotonic compression tests for sandy soil drainage with $Dr = 40\%$ and 60% are compared with numerical simulation results. Furthermore, Fig. 4 presents the response of excess pore water pressure (Δu), shear response, and stress paths in the undrained cyclic triaxial test for sandy soils with $Dr = 40\%$. The findings demonstrate that the proposed constitutive model effectively captures

the stress-strain behavior of sandy soils with varying relative densities, while also depicting the gradual development of excess pore water pressure (EPWP). The calibrated parameters of Nevada sandy soil, obtained through numerical simulation of triaxial tests, are presented in Table 2.

Comparison of calibration parameters P1 and P2 shows that the two dilatancy parameters, α_1 and α_3 , which are closely related to pore pressure and volumetric strain development, have a certain impact on the element. As α_1 increases and α_3 decreases, the rebound strain

Table 4

Main parameters and dimensions of the 10 MW DTU OWT model.

Component	Property	Value
Rotor-nacelle assembly (RNA)	Rating	10 MW
	Cut-in, rated, cut-out wind speeds	4 m/s, 11 m/s, 25 m/s
	Maximum, minimum rotor speeds	6.0 rpm, 9.6 rpm
	Rotor diameter	178.3 m
	Rotor mass	227,617 kg
	Nacelle mass	446,036 kg
	Single blade overall mass	40,699 kg
	Hub height	119 m
	Hub mass	105,520 kg
	Hub diameter	5.6 m
Tower	Tower integrated mass	786,223 kg
	Length of the tower	115.6 m
	Tower base diameter and thickness	10.375 m, 0.038 m
	Tower top diameter and thickness	6.875 m, 0.02 m
Supported foundation	Pile integrated mass	2,554,000 kg
	Length of the pile	75 m
	Monopile diameter and thickness	10.375 m, 0.125 m
	Length of embedded pile	35 m
	Density of supports structure	8500 kg/m ³
	Young's modulus	210 GPa

decreases, and pore pressure accumulation accelerates.

2.3. centrifugal test

In this paper, CSP3 centrifugal test data recorded by [Wilson, \(1998\)](#) was used for verification. The soil profile in this test comprises two horizontally layered and uniformly graded Nevada sands ($Cu = 1.5$, $D_{50} = 0.15$ mm). At the prototype scale, the upper loose sand thickness is 9.1 m, with a relative density (Dr) of 55 %, and a permeability coefficient of 6.05×10^{-5} m/s. While the lower dense sand thickness is 11.4 m, with $Dr = 80$ %, and a permeability coefficient of 3.70×10^{-5} m/s. The buried depth of the single pile is 16.8 m, the pile wall thickness is 0.019 m, and the outer diameter is 0.67 m. The upper structure is 3.8 m above the ground with a load of 480 kN. The centrifugal test adopts the 1995 Kobe seismic wave time history (see [Fig. 6](#)), with a peak acceleration of 0.22g. As shown in [Fig. 5](#), a three-dimensional finite element model was established at prototype scale according to the test to simulate the structure-pile-soil interaction. The specifics regarding the development of the numerical model, including interface elements and boundary conditions, are provided in Appendix A.

[Figures 7 and 8](#) show the time-history comparison of EPWP and acceleration response at different depths. The numerical results effectively reflect the pore pressure and acceleration response of soil layers with varying relative densities. [Fig. 9](#) compares the dynamic responses of the superstructure and pile foundation, validated by test data. The calculated results exhibit excellent consistency with the measured outcomes. These findings indicate that the numerical simulation method proposed in this paper can reliably predict the dynamic response of soil and piles under pile-soil interaction.

Results from P1 and P2 indicate that parameter adjustments have limited impact on the overall modeling. The differences in excess pore pressure, acceleration response, and pile dynamic response are minor, with both capturing consistent trends of pile-soil interaction. Although P2 offers better element-level calibration, the centrifuge test involves a more complex, non-uniform loading path compared to conventional uniform cyclic tests. Therefore, P1 was adopted for the subsequent 10 MW MOWT simulations.

Table 5

Simulation and description of different load types.

Load type	Load description	Calculation formula	Remark
Wind load	The wind load acting on the tower barrel	$F_{sh}(z) = 0.5\rho_a C_D D(V+v)^2$ (Binh et al., 2008)	ρ_a is the air density, assumed to be 1.225 at 15 °C and 1 atm; D is the tower's average diameter; $V_{(z)}$ and $v_{(z,t)}$ are the average and fluctuating wind speeds along the turbine tower height, respectively; C_D is the drag coefficient, set to 1.2 in this study.
	A wind load acting on blades	The top of the tower generates thrust in the windward direction. $F_T = 0.5\rho_a \pi R_T^2 V_s^2 (1 + 2v_s/V_s) C_T$ (Lee et al., 2010)	V_s and v_s are the average and fluctuating wind speeds at the hub, respectively; R_T is the blade radius; C_T is the thrust coefficient, calculated as $C_T = 4a(1-a)$, a is the axial induction factor. In this article, $a = 0.5$.
Wave load	The horizontal wave load of unit length dz acting on the pile foundation	Morrison formula $df = df_D + df_I = \frac{1}{2}\rho C_D D v_x v_x dz + \frac{\pi}{4}\rho C_M D^2 a_x dz$ (Cao et al., 2020)	df_D and df_I represent the velocity force and inertial force, respectively. Here, $\rho = 1030$ kg/m ³ is the seawater density; $C_D = 1.2$ is the drag coefficient, $C_M = 2.0$ is the mass coefficient; D is the tower body diameter; v_x and a_x are the horizontal velocity and acceleration of water particles. (Zuo et al., 2018)
Hydrodynamic pressure	Interaction between seawater and pile foundation	$m_a = C_a A_p \rho_w$ (Liaw and Chopra, 1974)	C_a is the additional mass coefficient. $C_a = 1.0$; ρ_w is the density of seawater; A_p is the cross-sectional area of the tower.
Seismic load	Earthquake acting on the base (bedrock) of the model	Seismic waves at TCU045 monitoring station in ChiChi area in 1999	The predominant frequency of the seismic wave is 2.2 Hz.

3. Finite element model of 10 MW MOWT

The dynamic response of MOWT in a liquefiable seabed under seismic and environmental loads is simulated using the numerical method described above. A brief overview of the establishment of the 3D finite element model of MOWT and the generation of loads is provided.

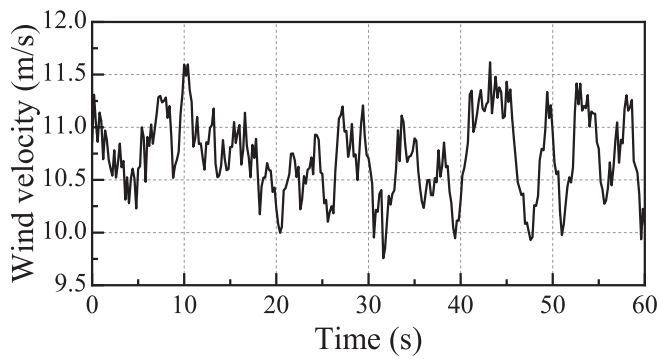


Fig. 11. Wind velocity time history curve in 113 m.

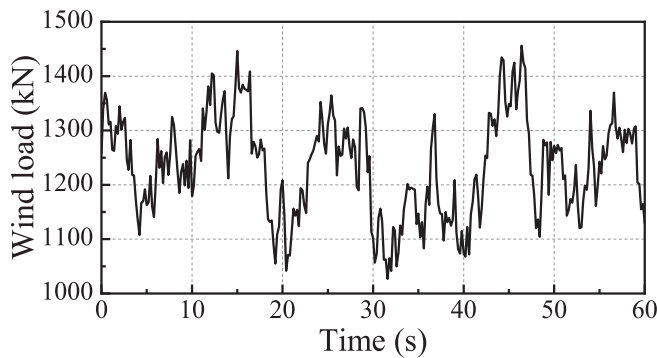


Fig. 12. Wind load time history curve at hub.

3.1. 3D finite element model

3.1.1. Sand soil

The seabed adopts the saturated Nevada sand mentioned above, and when the finite element soil domain is set to 20D (200 m) horizontally and 5D (50 m) vertically from the pile end, the influence of boundary effect on the calculation results can be basically eliminated. The final overall scale of the soil domain is $200\text{ m} \times 200\text{ m} \times 85\text{ m}$, and there are 17,648 elements. The mesh distribution is shown in Fig. 10(b). To improve computational efficiency and ensure accuracy, the SBFEM-FEM coupling analysis method of saturated porous media (Zou et al., 2019; Chen et al., 2018) is combined with octree discretization technology for cross-scale modeling (Chen et al., 2021; Nie et al., 2022; Chen et al., 2023). The mesh near the pile foundation is locally refined in the radial direction, with denser mesh division within 1.5D from the pile center. The transition elements are modeled using the high-precision Scaled Boundary Finite Element Method (SBFEM), a semi-analytical, high-accuracy numerical approach that employs circumferential discretization

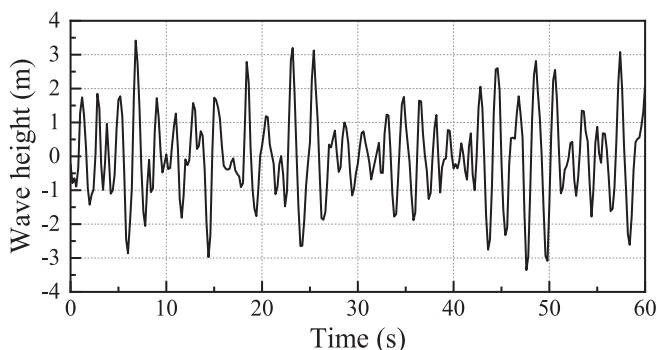


Fig. 13. Wave height time history curve.

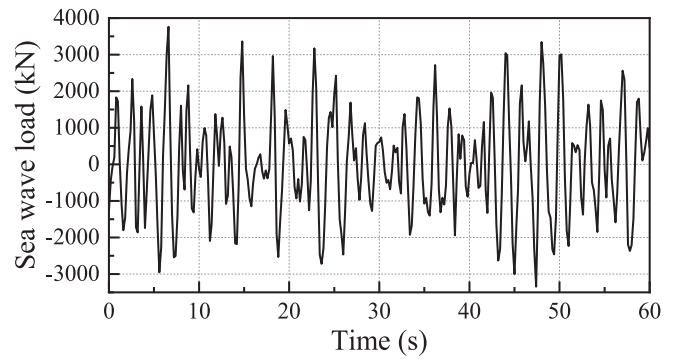


Fig. 14. Typical wave load time history curve.

and radial analytical solutions. By combining the advantages of the Finite Element Method (FEM) and the Boundary Element Method (BEM), SBFEM is well-suited for solving problems involving finite domains, infinite domains, and multiscale systems. In this study, the scale difference between the pile foundation and the soil domain exceeds two orders of magnitude, and the use of SBFEM enables efficient multiscale analysis (Song and Wolf, 1997; Zhang et al., 2022a,b). As illustrated in Fig. 5, the transition element comprises 9 faces and 13 nodes, while Fig. 10 shows that the transition element consists of 7 faces and 10 nodes. The remaining soil domain is modeled using conventional 8-node hexahedral elements.

3.1.2. 10 MW OWT model

The parameters of the 10 MW OWT are listed in Table 4. The pile foundation has a diameter of 10 m and a burial depth of 35 m. The rotor nacelle assembly (RNA) is simplified in this study. Fig. 10(a) illustrates the working environment and dimensions of the MOWT system, which includes 8-node hexahedral elements for the dispersed piles and the upper structure, with a total of 2824 elements (see Fig. 10(b)). The pile and tower are modeled using a linear elastic model, with a Young's modulus of 210 GPa, a density of 7800 kg/m^3 and Poisson's ratio of 0.3. The method of equivalent stiffness ($E_{sp}I_{sp} = E_{hp}I_{hp} - E_{cs}I_{cs}$) and equivalent density ($\rho_{sp}A_{sp} = \rho_{hp}A_{hp} + \rho_s(A_{sp} - A_s)$) addresses the issues of small pile wall size and large pile-soil stiffness differences. Here, E_{sp} , I_{sp} , ρ_{sp} , and A_{sp} represent the elastic modulus, moment of inertia, density, and cross-sectional area of the hollow pile; E_{hp} , I_{hp} , ρ_{hp} , and A_{hp} are the corresponding parameters for the solid pile; E_{cs} and I_{cs} are the average elastic modulus and moment of inertia of the soil at the embedded depth; ρ_s is the soil density. The monopile foundation and tower barrel are modeled as an equivalent cylinder, similar to studies by Achmus et al. (2009) and Page et al. (2021). The equivalent solid pile has a density of 402.8 kg/m^3 and Young's modulus of 19.5 GPa, while the equivalent solid tower barrel has a density of 114.8 kg/m^3 and Young's modulus of 5.59 GPa.

3.1.3. Pile-soil interaction

The pile-soil interaction is modeled using the zero-thickness generalized plastic contact surface model (Liu et al., 2014). Teng (2023) calibrated the interface parameters by building upon Tran (2005)'s research and successfully applied these parameters to the suction bucket model in sandy soil. The finalized parameters are presented in Table 3.

3.1.4. Boundary conditions

To simulate the undrained conditions of sands during an earthquake, impermeable boundaries are applied to the bottom and sides, while the top boundary is permeable. The bottom boundary condition is fully fixed in all directions. For the side boundaries, a equivalent displacement constraint is implemented to simulate seismic wave propagation in the X-direction; this ensures that nodes at the same elevation on both sides of the model have identical displacements, thereby preventing the

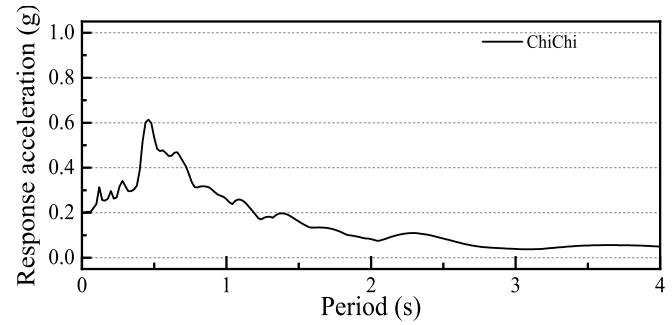
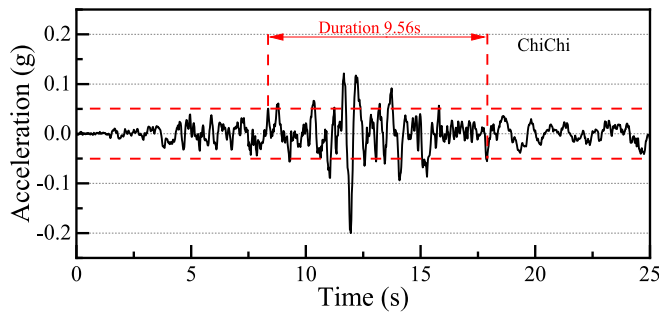


Fig. 15. Acceleration time history and response spectra for the earthquake record.

Table 6

List of working conditions in the numerical simulation.

Cases	Mesh type	Load type	Dr (%)	Rd	PGA (g)	Capacity (MW)
1	SBFEM-FEM	Wind + Wave + Seismic	55 + 80	0.35	0.2	10
2	FEM	Wind + Wave + Seismic	55 + 80	0.35	0.2	10
3	SBFEM-FEM	Wind + Wave	55 + 80	0.35	—	10
4	SBFEM-FEM	Seismic	55 + 80	0.35	0.2	10
5	SBFEM-FEM	Seismic	55 + 80	0.35	0.4	10
6	SBFEM-FEM	Wind + Wave + Seismic	55 + 80	0.35	0.4	10
7	SBFEM-FEM	Wind + Wave + Seismic	80 + 80	0	0.2	10
8	SBFEM-FEM	Wind + Wave + Seismic	40 + 80	0.35	0.2	10
9	SBFEM-FEM	Wind + Wave + Seismic	40 + 80	0.65	0.2	10
10	SBFEM-FEM	Wind + Wave + Seismic	55 + 80	0.65	0.2	10
11	SBFEM-FEM	Wind + Wave + Seismic	40 + 80	1	0.2	10
12	SBFEM-FEM	Wind + Wave + Seismic	55 + 80	1	0.2	10
13	SBFEM-FEM	Wind + Wave + Seismic	40 + 80	0	0.2	5
14	SBFEM-FEM	Wind + Wave + Seismic	40 + 80	0.23	0.2	5
15	SBFEM-FEM	Wind + Wave + Seismic	40 + 80	0.54	0.2	5
16	SBFEM-FEM	Wind + Wave + Seismic	40 + 80	1	0.2	5

reflection of seismic waves.

3.1.5. Damping

In MOWTs, the total damping is the linear sum of structural, aerodynamic, hydrodynamic, and soil dampings (Mehravar et al., 2016; Eslami and Ghorbani, 2022). For this study, the structural damping ratios for the wind turbine blade and tower are 3.5 % (Kühn, 2001) and 1.36 % (Damgaard and Andersen, 2012), respectively. The hydrodynamic damping ratio is 0.15 % (Germanischer, 2010), and the soil damping ratio is 5 %.

3.2. Loading type

The calculation of wind load and wave load in this paper has been published in the author's previous studies (Cheng et al., 2023) and will not be repeated here but is briefly described using lists and illustrations. Table 5 details the load types, and Fig. 11 presents the simulated time-history curve of average wind speed. Fig. 12 illustrates the simulated

wind speed time-history curve at the hub for a wind speed of 10 m/s. Using a water depth of 40 m as an example, Fig. 13 provides the simulated time-history curve of effective sea-level wave height. Additionally, Fig. 14 displays the simulated time-history curve of a typical wave load when the effective wave height is 5 m. In this study, seismic waves recorded at the TCU045 monitoring station in the ChiChi area in 1999 were selected. The prominent frequency of these seismic waves is 2.2 Hz, as shown in Fig. 15.

3.3. Numerical simulation condition

Firstly, the accuracy and efficiency of the saturated porous media coupled SBFEM-FEM method (Cases 1–2) are studied. Secondly, the degree of influence of different loads on the dynamic response and liquefaction of MOWT is investigated. Five working conditions (Cases 1, 3–6) are defined in the numerical simulation to analyze the development and distribution of pore pressure and to reveal the failure mode of MOWT in the liquefiable seabed. Next, parametric studies were conducted to evaluate the effects of the relative depth (Cases 1, 7–12) is examined. The relative depth (Rd) of liquefiable sand is defined as $Rd = H_{liq}/H_{emb}$, where H_{liq} denotes the thickness of the liquefiable loose sand layer, and H_{emb} represents the monopile embedment depth. Finally, to investigate the impact of the large-scale trend, a comparative analysis was conducted between 10 MW and typical 5 MW MOWT (Cases 13–16). See Table 6 for specific calculation examples.

In the initial stage of analysis, gravity is applied to the seabed to establish an initial stress equilibrium. In the second step, the central soil mass is excavated, MOWTs are installed at the designated positions, and gravity is reapplied to re-establish the stress equilibrium. Finally, in the third step, the effects of varying load conditions and different relative depths of liquefiable loose sand on MOWTs are investigated.

4. Results and discussion

In this section, we compare the advantages of the SBFEM-FEM coupling analysis method. We analyze the effects of various loads and different Rd values on the temporal and spatial variation patterns of pore pressure. Additionally, we examine dynamic responses including horizontal displacement, acceleration and rotation angle in MOWT. The pile-soil flow mechanism of liquefiable seabed is elucidated, and the impact of the trend toward larger wind turbines is examined.

4.1. Comparison of methods

To demonstrate the high efficiency of this method, various grid models of identical dimensions were compared. Fig. 16(a), on the other hand, illustrates the SBFEM-FEM coupling analysis model, comprising a total of 20,976 elements. In this model, the soil is characterized by 17,072 solid elements, 576 transition elements, and 776 pore pressure degrees of freedom. Fig. 16(b) illustrates the finite element (FEM) model, discretized into 37,776 elements. The soil domain comprises

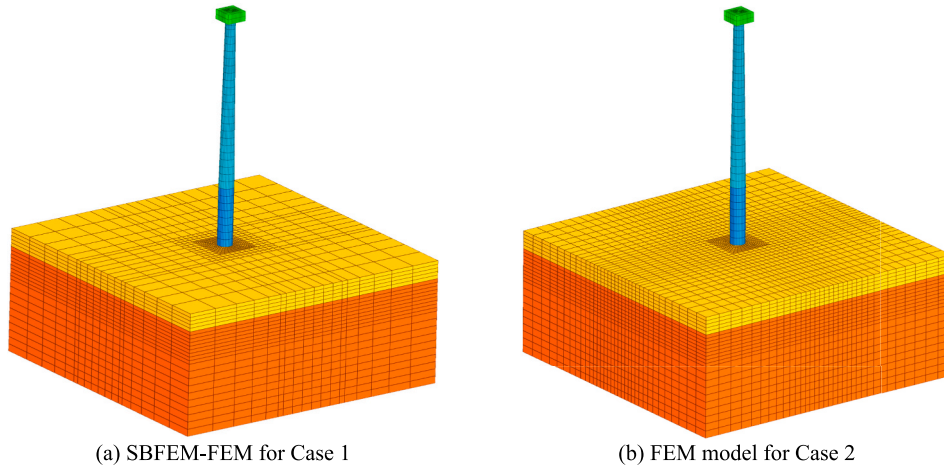


Fig. 16. Comparison of 3D finite element models.

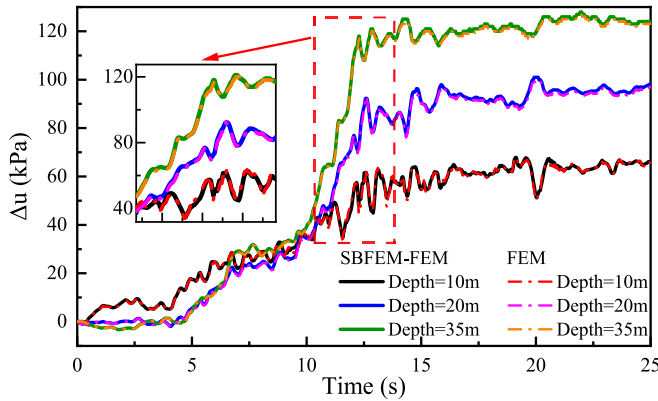


Fig. 17. Comparison of Δu -time history at different monitoring points (Range = 3.2D).

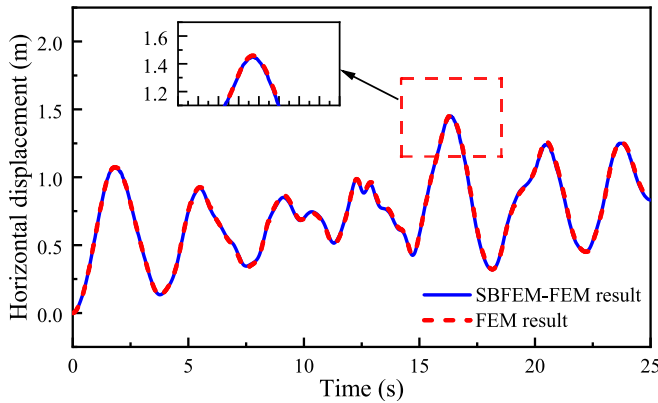


Fig. 18. Comparison of RNA displacement-time history.

34,448 solid elements with 1496 pore pressure degrees of freedom.

Figures 17 and 18 shows the comparison of the pore pressure and RNA displacement calculation results at different depths for the two meshes. Fig. 19 illustrates the comparison of accelerations at various positions of the pile foundation between the two models. The results indicate that the pore pressure, displacement and acceleration response of the SBFEM-FEM model are consistent with those of the FEM mesh model. The calculation time for the former is 18 h, while that for the latter is approximately 30 h. Therefore, by using this method, not only is

the calculation accuracy guaranteed, reflecting the dynamic response and pore pressure development trend of the soil-pile foundation, but also the calculation efficiency of the same model can be increased by 40 %.

4.2. EPWP response

In the sandy seabed surrounding MOWTs, the evolution of pore pressure is a critical factor influencing strength changes under diverse dynamic loads and is essential for stability analysis using the effective stress method. In this paper, the excess pore water pressure ratio (ru) is defined as the ratio of excess pore water pressure to initial vertical effective stress (Madabhushi et al., 2010), $ru = \Delta u / \sigma'_{v0}$, where Δu is the current EPWP, σ'_{v0} is the initial vertical effective stress. The region with $ru \geq 0.8$ at the end of the earthquake is regarded as a liquefaction region (Beatty and Byrne, 2011).

Fig. 20 shows the excess pore pressure ratio (ru) time-histories under different loads. Under high-intensity seismic loading, the soil near the pile foundation, at distances of 1D and 1.9D (where D represents the pile diameter), has experienced varying degrees of pore pressure accumulation. The peak ru values reach 0.37, 0.94, and 1.0 for environmental loading (Case 3), seismic loading (Case 5), and combined environmental-seismic loading (Case 6), respectively. In contrast, the ru values at greater distances from the pile foundation (3.2D and 4.8D) exhibit distinct trends. Under environmental loading alone, pore pressure accumulation is minimal due to limited pile-soil interaction and minimal soil disturbance, which prevents rapid pore pressure buildup. However, even under low-intensity seismic loading (Case 5), the excess pore pressure at the far-field location (peak $ru = 0.76$) exhibited rapid accumulation, significantly increasing liquefaction potential. When environmental and seismic loads act concurrently (Cases 1 and 6), the trend in pore pressure development closely resembles that observed under seismic loading alone (Case 4 and 5). Comparative analysis demonstrated that seismic loading substantially reduces soil stiffness and markedly accelerates sand liquefaction when compared to environmental loading alone.

All working conditions suggest that for soil near the foundation, the cumulative changes in oscillatory pore pressure and residual pore pressure are substantial. The influence range of pile-soil interaction on pore pressure is approximately within 3.2D. Beyond this range, the development trend of pore pressure in the soil remains largely consistent. Furthermore, increasing the amplitude of ground motion results in a more pronounced liquefaction effect, causing greater oscillation in the pore pressure ratio around the pile.

Fig. 21 shows the ru profiles at 25 s for different ranges under three loading conditions. It can be observed that, in Case 3, ru gradually increases with soil depth and reaches its maximum near the shallow

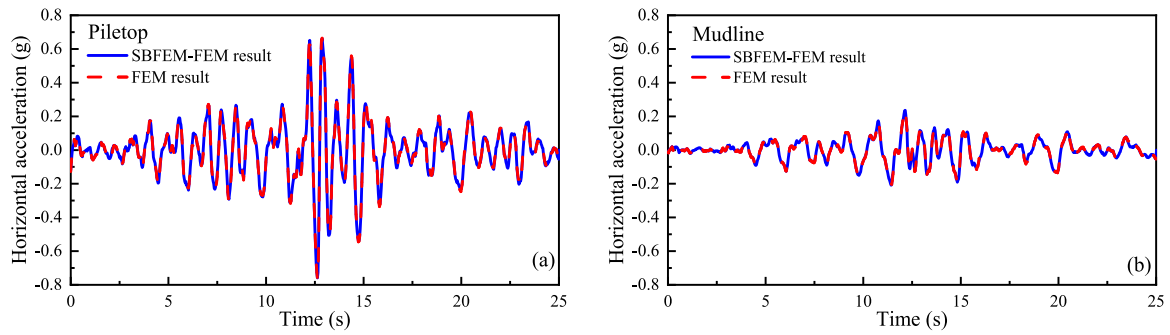


Fig. 19. Comparison of acceleration time-history curves at different monitoring points of monopile.

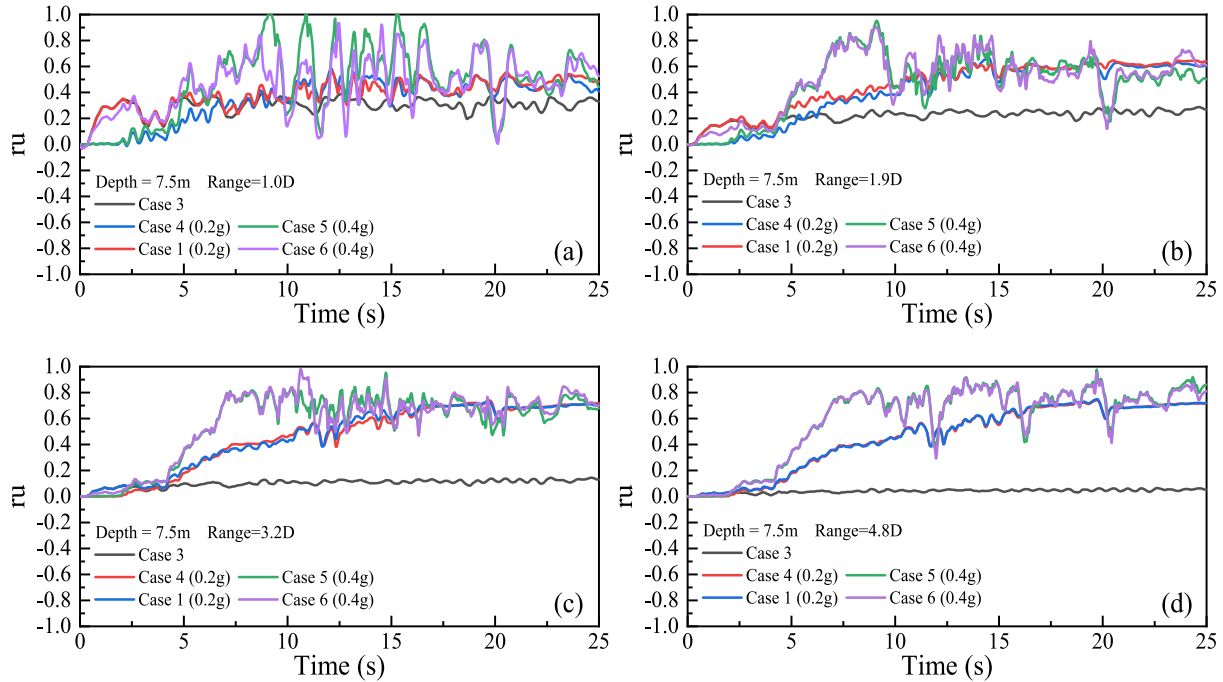


Fig. 20. Ru time history curves for different loading cases.

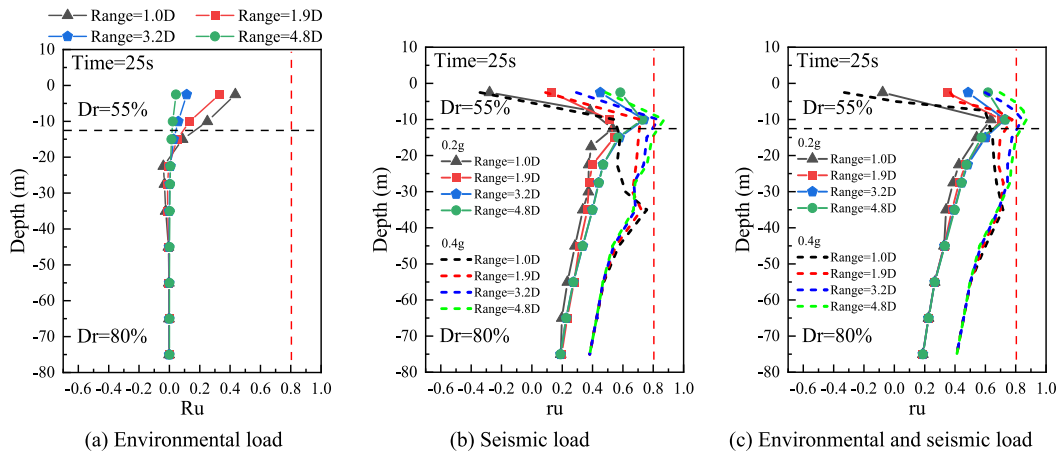


Fig. 21. Ru profiles at different monitoring points for different loading cases.

surface. Under a seismic load of 0.2 g, Cases 1 and 4 show that ru first increases and then decreases with soil depth, peaking within the liquefiable soil layer.

Notably, under a seismic load of 0.4 g, a distinct inflection point in the ru profile appears near the pile toe (-35 m). At the same depth, ru is highest near the pile (black line) and then decreases; conversely, it

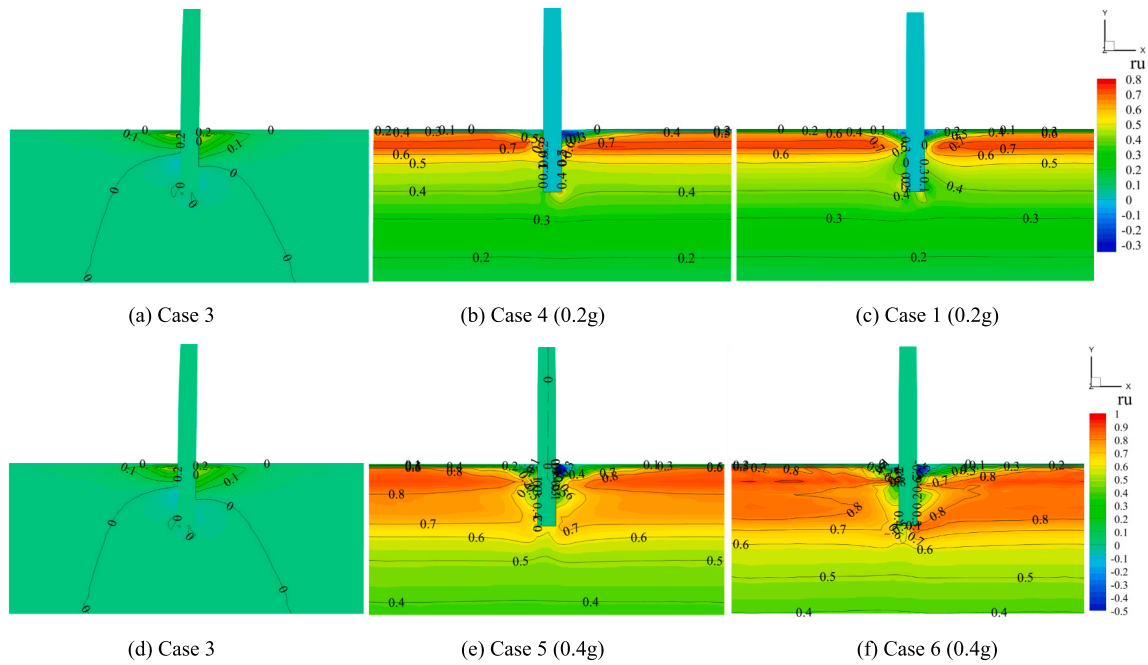


Fig. 22. Ru contour cloud map under different loads (25 s).

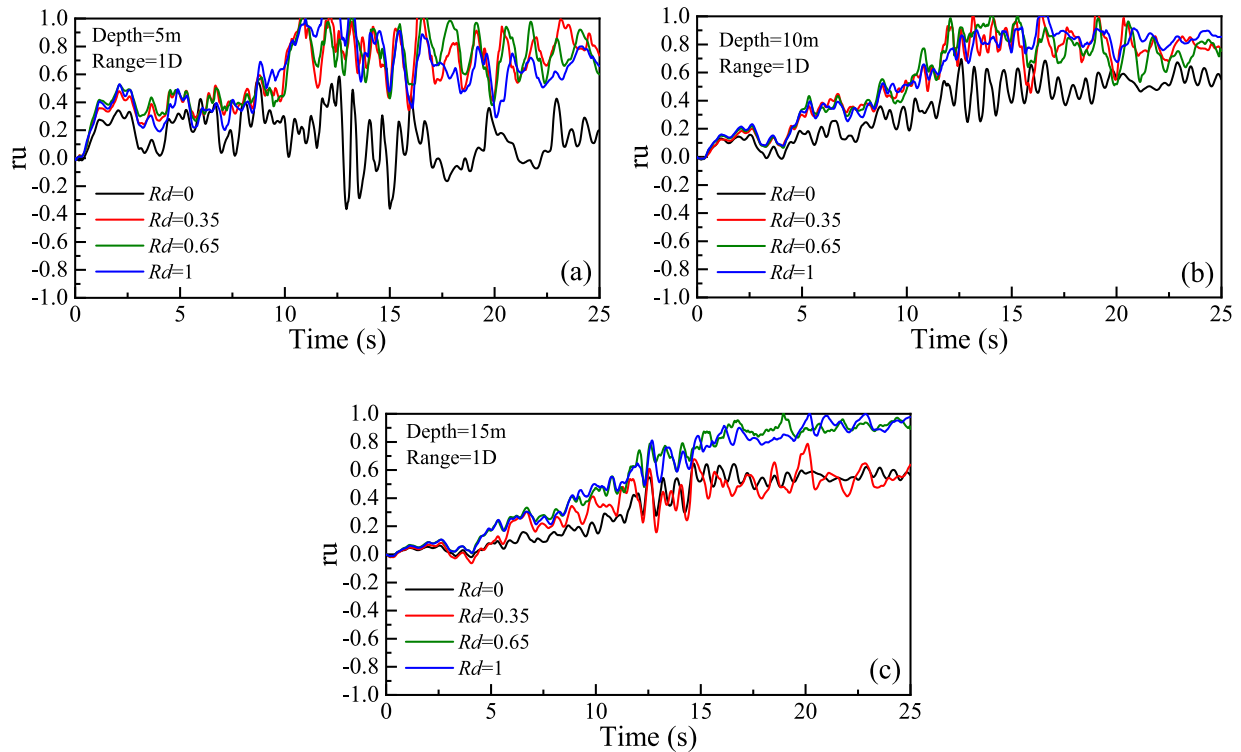


Fig. 23. Comparison of ru development at 1D of different liquefaction depths of $Dr = 40\%$ sandy soil.

increases away from the pile (green line). This is because the increase in seismic intensity led to severe inclination of the pile foundation and significant pile-soil interaction at the pile toe, resulting in substantial accumulation of pore pressure at this location.

Fig. 22 presents the contour plot of ru at this moment. It can be observed that under a PGA of 0.4 g, it can be observed that under 0.4 g, the extent of seabed weakening is broader, with ru exceeding 0.7 near the pile toe. Under a PGA of 0.2 g, the weakening is primarily confined to the upper loose sand layer, with ru around 0.7.

To investigate the influence of liquefiable soil layer depth on MOWTs, with a seismic input of 0.2 g and an overlying sand layer of $Dr = 40\%$ as an example, Figs. 23 and 24 illustrate the time-history curves of ru at various depths near (1D) and far from (3.2D) the pile under different Rd conditions. This figure indicates that in the models with $Rd = 0.35, 0.65$, and 1, the soil liquefies approximately at 11 s, resulting in large horizontal displacements and deflections of MOWT (see Sections 4.3). In the dense sand with $Rd = 0$ ($Dr = 80\%$), the development trend of ru is similar to that of loose sand, but ru does not exceed 0.8 whether

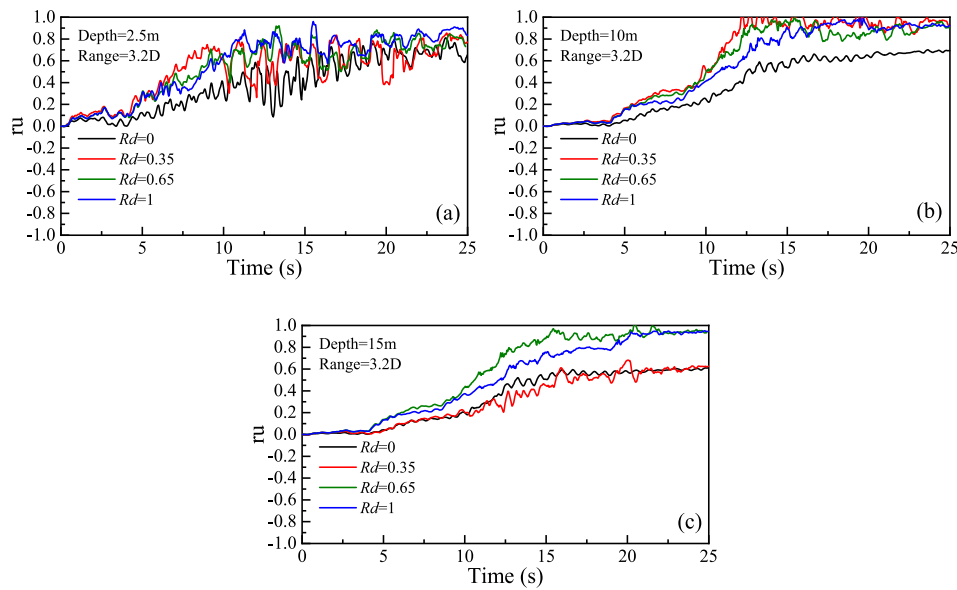


Fig. 24. Comparison of ru development at 3.2D of different liquefaction depths of $Dr = 40\%$ sandy soil.

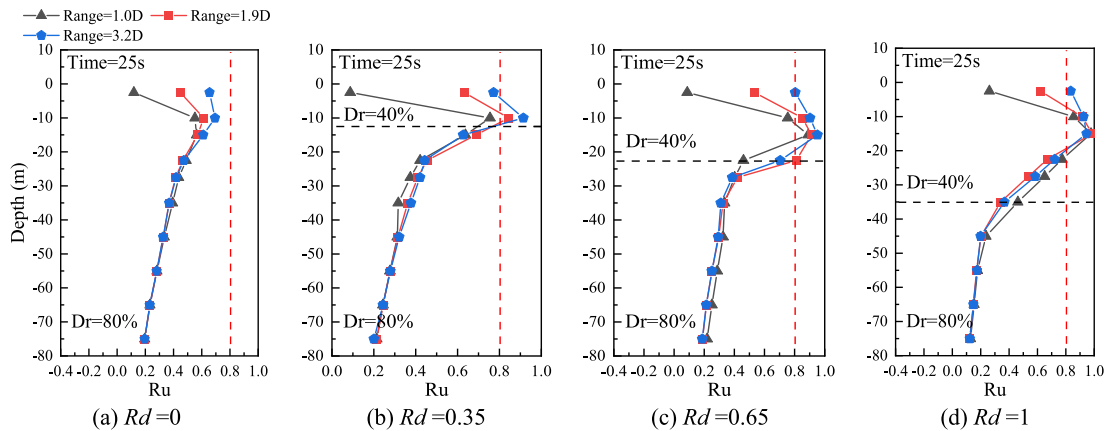


Fig. 25. Ru profiles at different monitoring points for the different R_d .

at the position near the pile or far from the pile. The vibrating pore pressure of the soil at the position far from the pile is small, and the accumulated pore pressure is high. The pore pressure near the pile gradually tends to be stable and changes reciprocally with vibration, and the soil shows certain dilatancy, showing obvious cyclic liquefaction.

Fig. 25 shows the ru profiles of soil with different R_d ranges at 25 s. Since pore pressure trends after 3.2D are similar, only three ru data columns are displayed. The results indicate that the depth and extent of soil liquefaction increase with the rise in R_d . However, when R_d reaches 1, not all liquefiable soil layers undergo liquefaction, and the liquefaction depth stabilizes at approximately 22.5 m. By comparing Fig. 25(c) and (d), we observe that the liquefiable soil layer comprises a large proportion. When R_d exceeds 0.65, increased confining pressure and energy loss from seismic waves prevent further increase in liquefaction depth. However, for soil between 22.5 m and 35 m, the ru remains relatively high, indicating significant soil weakening. Comparison of Figs. 21(c) and 25(b) shows that, at the same liquefiable depth, reducing the relative density of sand increases the pore pressure ratio and the liquefaction tendency of the soil.

4.3. Horizontal displacement response

For the design of OWTs, foundation deformation is more critical than

ultimate bearing capacity (Byrne et al., 2010). Under the serviceability limit state (SLS), the mudline deflection of a monopile should be less than 1/500 of the embedment depth (Germanischer, 2010). The maximum deflection at the tower top should be limited to within 1.25 % of the tower height to prevent excessive deformation (Nicholson, 2011).

Comparing Fig. 26(a) and (b), it can be observed that the amplitude of horizontal displacement at various locations of the MOWTs increases with the seismic intensity. Environmental loads primarily contribute to the cumulative horizontal displacement of MOWTs. Earthquake loads reduce the stiffness of the soil surrounding the piles. The combined action of environmental load and seismic load (Case 1) amplifies the lateral horizontal displacement of the MOWTs, causing not only the pile foundation to exceed the threshold but also the tower top horizontal displacement to reach the SLS limit.

As observed from the deflection envelope in Fig. 26(c), the horizontal deflection of the MOWTs increases with height, reaching its maximum at the tower top. Under seismic load (Cases 4 and 5), the MOWTs exhibit relatively elastic and symmetrical deformation characteristics, while environmental load (Case 3) gradually accumulates towards one side. Compared to Case 4 and Case 5, the horizontal deflection curves of Case 1, Case 3 and Case 6 are minimal in the negative direction. As the seismic intensity increases, the positive deflection of the pile foundation and tower increases with seismic intensity.

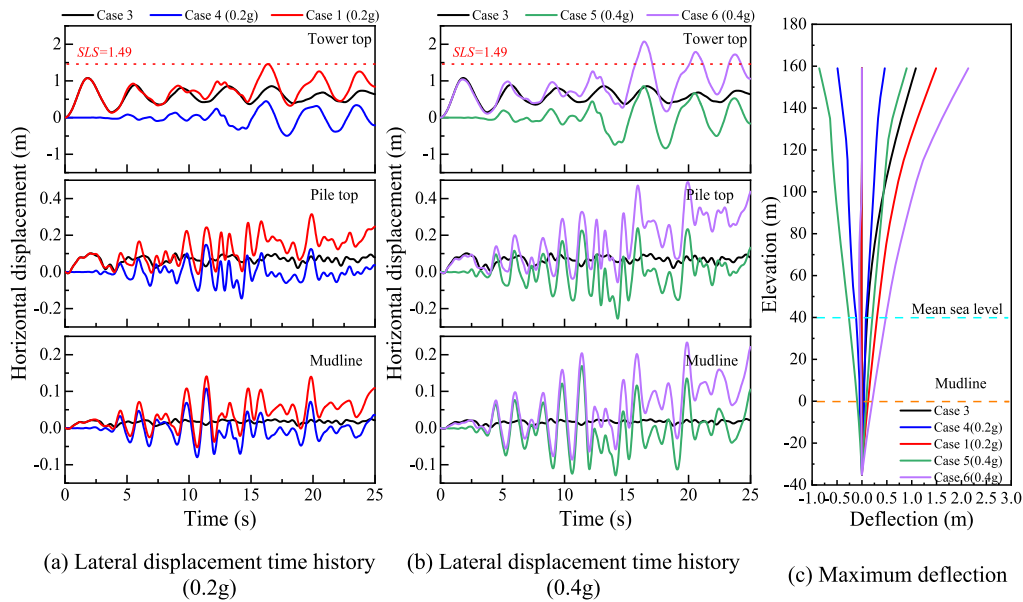


Fig. 26. Horizontal deformation of MOWT under different loads.

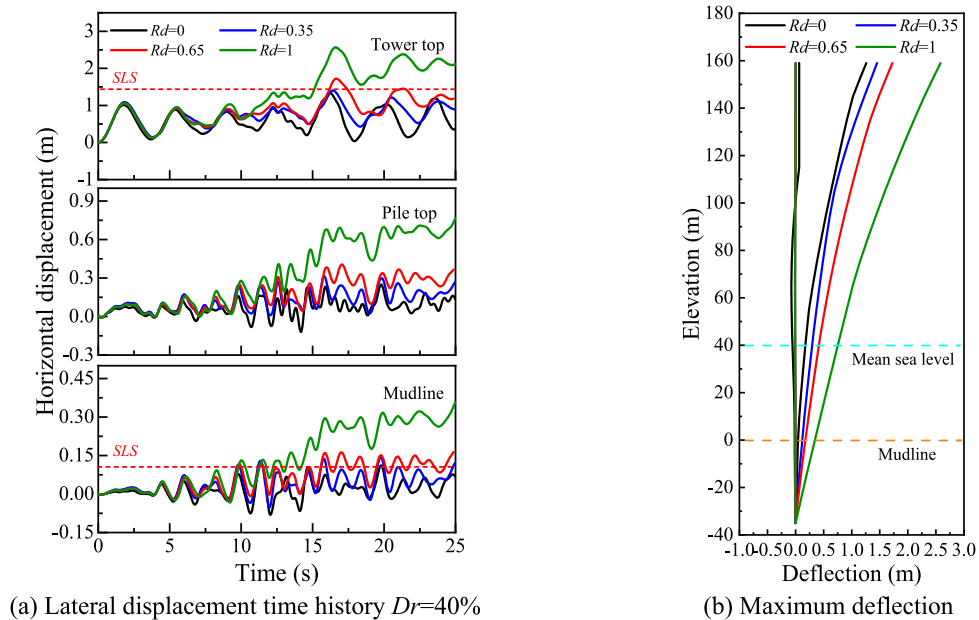


Fig. 27. Horizontal deformation of MOWTs in different R_d ($Dr = 40\%$).

Below the mean sea level (MSL), the peak deflection induced by a 0.2 g seismic load is approximately 50 % greater than that caused by environmental load alone. This further indicates that the liquefaction response induced by the earthquake significantly weakens the soil stiffness, resulting in larger deformations of the pile foundation.

Figures 27 and 28 present the time histories of horizontal deformation and peak deflection envelopes for MOWTs at different relative depths. As shown in the figures, the horizontal displacement of various positions of the MOWTs increases significantly after 6 s, primarily due to the substantial increase in pore pressure ratio, which reduces soil resistance. Except when $R_d = 0$, peak displacements at the mud surface exceed SLS in other cases. Comparing Figs. 27(b) and 28(b), it can be observed that the deflection deformations at various positions increases with increase of R_d . As R_d increases, the deflection deformation below the mud surface becomes progressively more linear.

4.4. Acceleration response

Fig. 29 shows the acceleration responses of MOWT under different loads. Results indicate that seismic load causes the most significant acceleration compared to wind and wave loads, significantly affecting tower vibration. The peak acceleration response lags with height changes. The acceleration amplification factor, defined as the ratio of output to input peak acceleration of the bedrock, is illustrated in Fig. 29 (b). Below the mudline, the factors increase monotonically for all conditions. Above the mudline, the variation trends of the acceleration amplification factor under seismic loading and wind-wave-seismic loading are similar, reaching the maximum value around 105 m. The acceleration amplification effect on MOWTs is more pronounced under low-intensity earthquakes. For example, in Case 1 and Case 6, the tower amplification factor induced by the 0.2 g seismic motion is 8.4, whereas it is 5.4 under the 0.4 g seismic motion.

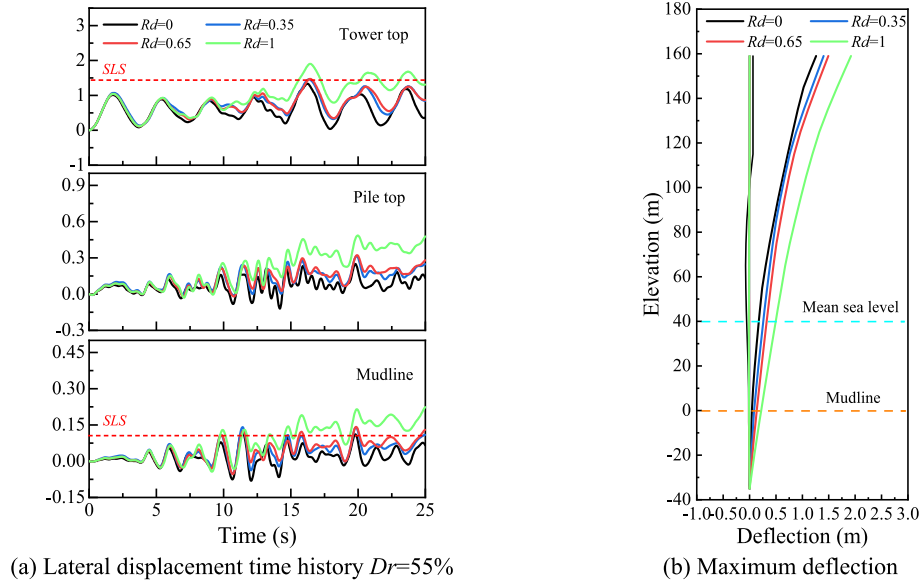


Fig. 28. Horizontal deformation of MOWTs in different R_d ($Dr = 55\%$).

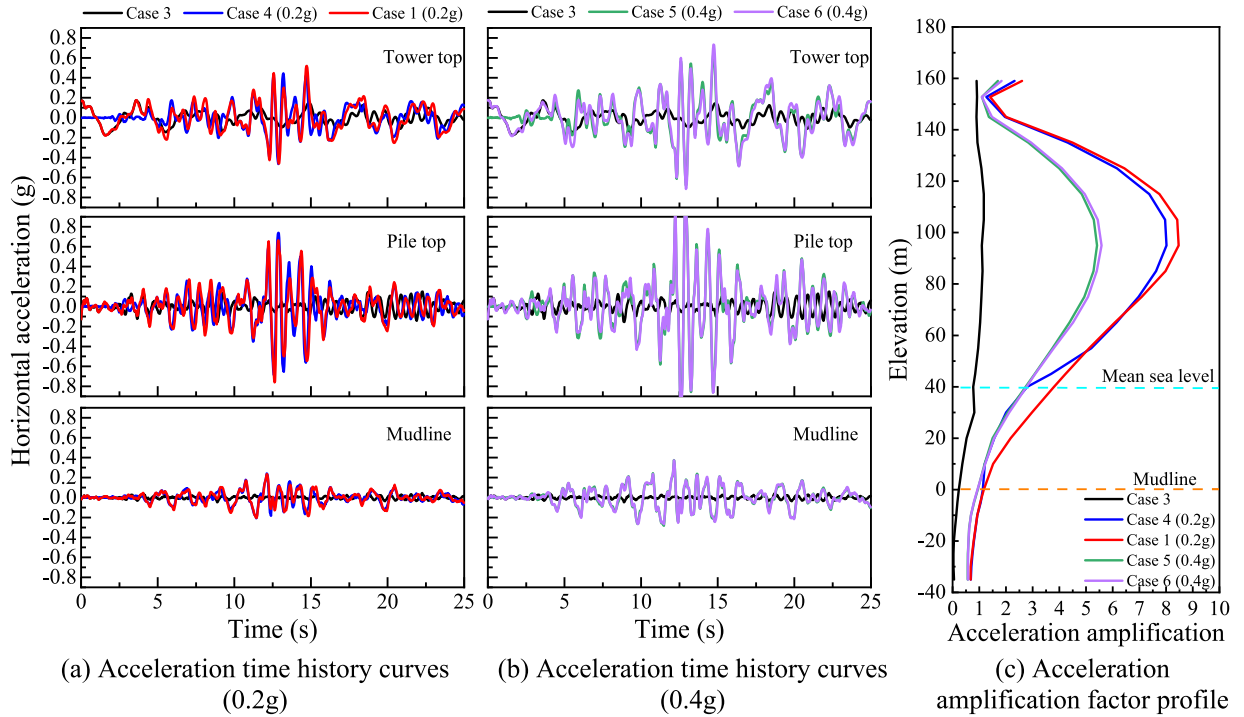


Fig. 29. Acceleration response of different loads.

Figs. 30 and 31 show the acceleration time histories at the mud surface, pile top, and tower top under various R_d conditions. Figs. 30(b) and 31(b) present the distribution of the acceleration amplification factor from the pile bottom to the tower top. Below the mudline, the factor increases monotonically when $R_d < 0.65$, but decreases first and then increases when $R_d > 0.65$. Above the mudline, the trends are similar across all conditions, peaking at around 100 m and decreasing as R_d increases. The increase in relative density (Dr) amplified the acceleration response at the top of the tower, potentially damaging the RNA.

4.5. Rotation response

At the serviceability limit state (SLS), the permanent accumulated

rotational angle at the mudline should not exceed 0.25° (Det Norske Veritas (DNV), 2013). Fig. 32(a) shows the time-history curves of the rotation angle at the mud surface of the pile foundation under different loads. Case 3 exhibits a more elastic response with a larger vibration rotation angle compared to Case 4, which has the smallest cumulative rotation angle of 0.06° . Case 1 shows significant rotation with a peak angle of 0.22° . Earthquakes influence the vibration and peak rotation angles, while environmental loads affect the cumulative rotation angle. As seismic intensity increases, pile foundation rotation becomes more noticeable. The combined effects of environmental and earthquake-induced seabed liquefaction significantly increase the cumulative rotation angle at the mud surface.

From Figs. 33 and 34, for both loose sand ($Dr = 40\%$) and medium-

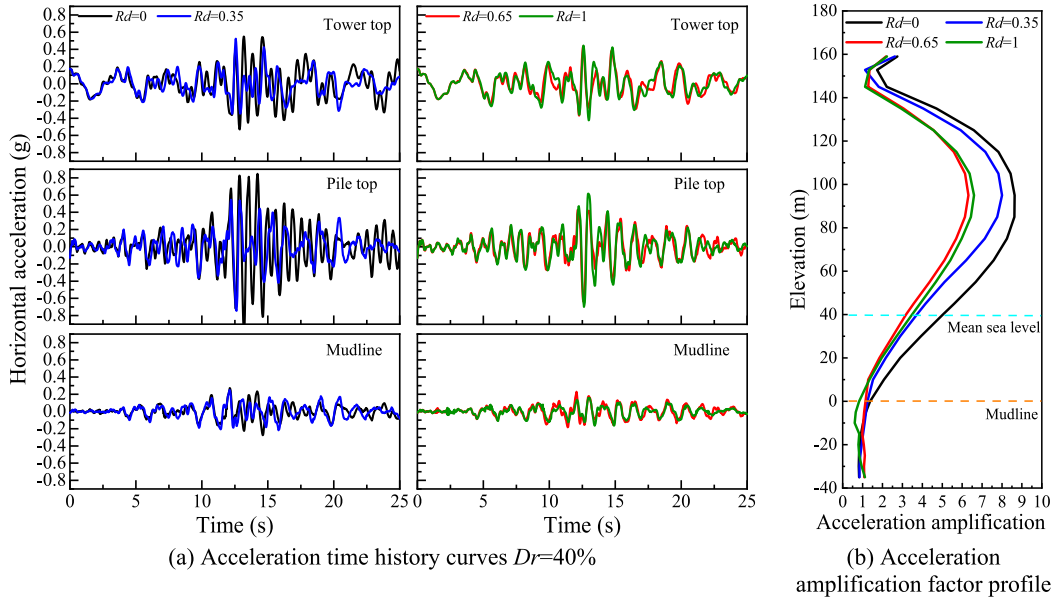


Fig. 30. Acceleration response of different R_d ($Dr = 40\%$).

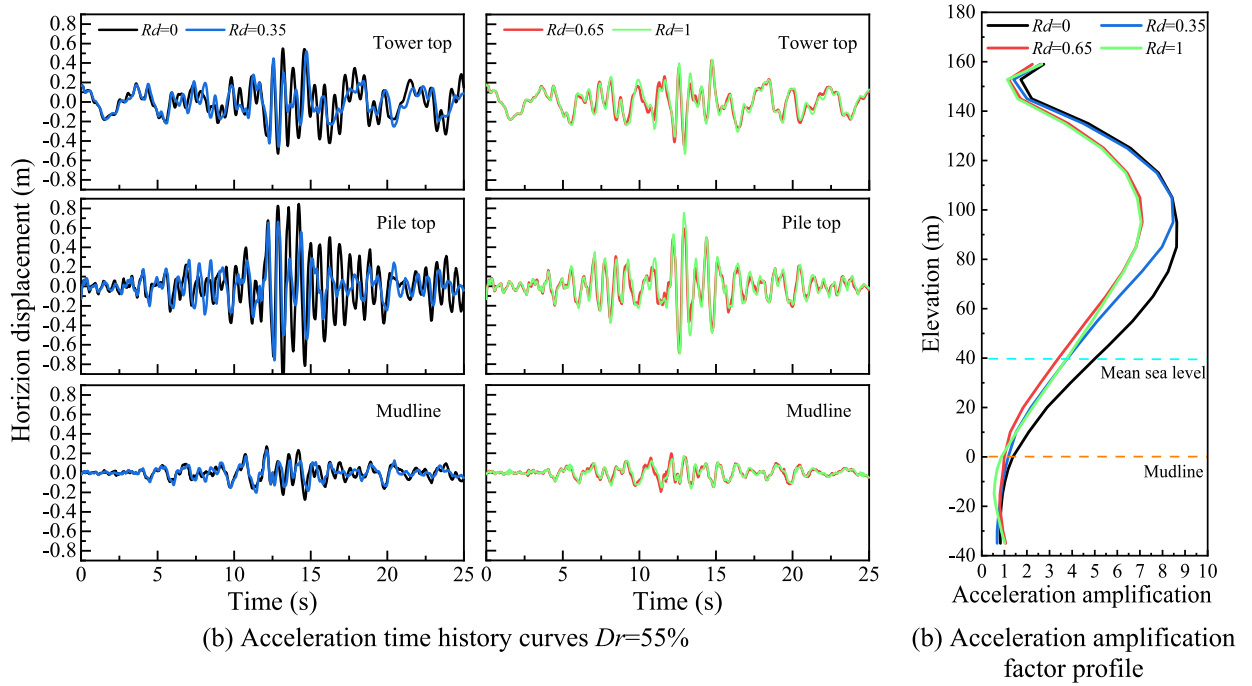


Fig. 31. Acceleration response of different R_d ($Dr = 55\%$).

dense sand ($Dr = 55\%$), the rotation angle increases with R_d . Comparing Figs. 33(b) and 34(b), the rotation angle decreases as the relative density of sand increases. When $R_d = 0.35$, neither peak nor cumulative rotation angles at the mud surface exceed 0.25° . For sandy soil, when $Dr = 55\%$ and $R_d = 0.65$, the pile foundation remains safe. However, when $Dr = 40\%$ of sandy soil and $R_d = 0.65$ and 1, the whole pile body rotates seriously and there is a risk of failure. For the soil layer conditions discussed in this article, the relative depth of the liquefiable soil layer in the 10 M MOWT should be controlled within 0.35.

4.6. Pile-soil flow mechanism

Fig. 35 illustrates the flow mechanism of the liquefiable seabed

around the pile under environmental loads. Due to the influence of environmental loads, the soil in front of the pile experienced collapse, while the soil behind the pile formed a “crescent-moon shape” mound as a result of the interaction between the pile and the surrounding soil. Within the initial 13.65 s, the soil deformation within the 1D range remained centrosymmetric. Subsequently, the subsidence area in front of the pile expanded, and the uplift behind the pile gradually increased until it eventually stabilized.

Fig. 36 illustrates the flow mechanism of the liquefiable seabed around the pile under seismic loads. After 10 s, seismic forces dominate, causing the soil around the pile to gradually flow sideways. The soil in front of the pile subsides, and the “crescent-moon shape” uplift disappears, leading to settlement. Seismic acceleration propagation

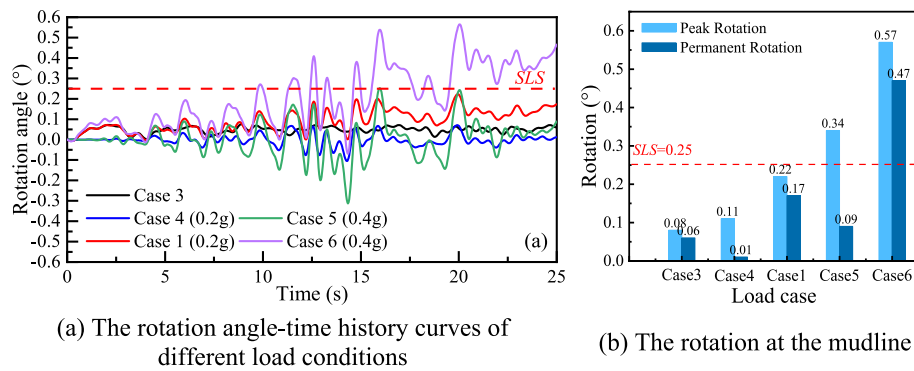
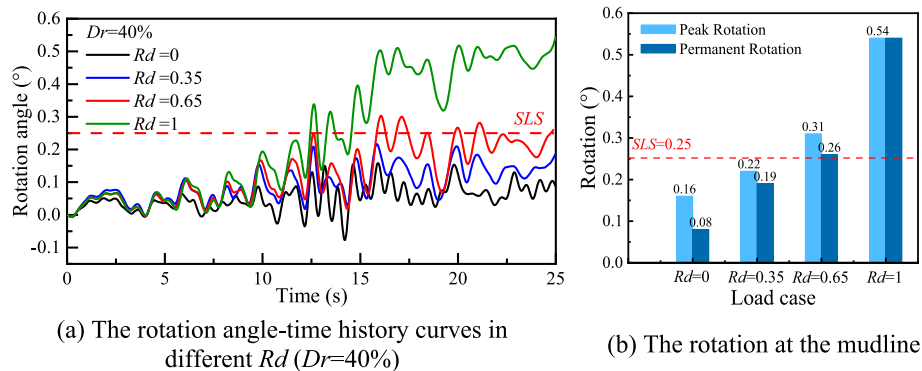
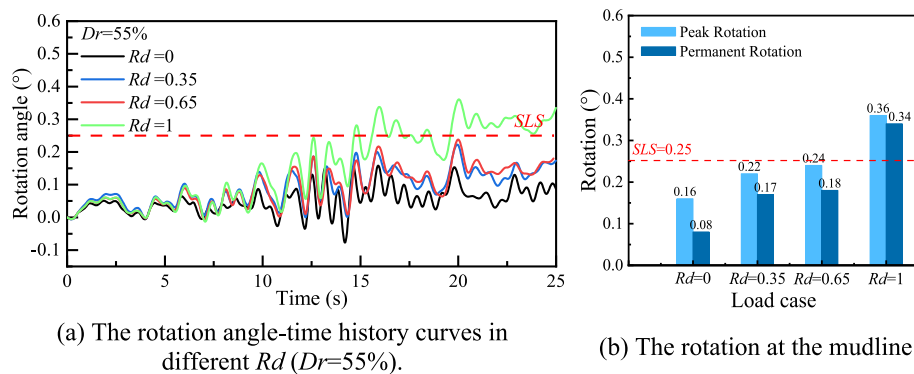


Fig. 32. Rotation angle response at the mud line of different loads.

Fig. 33. Rotation angle response of different R_d at the mud line ($D_r = 40\%$).Fig. 34. Rotation angle response of different R_d at the mud line ($D_r = 55\%$).

influences soil diffusion behind the pile. When motion aligns with acceleration, soil spreads sideways; otherwise, a “reflux” occurs. This repetitive motion causes significant settlement within 1D around the pile, uplift on both sides, and excessive rotation at the mudline, leading to damage.

Fig. 37 illustrates the flow pattern of the liquefiable seabed around the pile under wind-wave and seismic loads. In the first 5 s, seismic effects are minor, while environmental loads dominate. The soil in front of the pile collapses, forming a “crescent-moon shape” hillock behind the pile due to pile-soil interaction (see Fig. 38(a)). These observations align with findings by Cuéllar et al. (2012a) and Li et al. (2020). Fig. 38(b) shows Cuéllar et al. (2012a) scanning results, simulating sand deformation around a single pile with $D = 7$ m under cyclic loading.

When the seismic load dominates (after 10 s), the “crescent-moon shape” uplift of the soil behind the pile disappears, the soil within 1.5D around the pile settles, and the soil on both sides moves reciprocally to

form uplift, as shown in Fig. 39(a). This pattern holds for other seismic conditions, so no additional figures are provided. Settlement and uplift magnitude increase significantly with R_d .

Fig. 39(b) illustrates the multi-beam measurement results from a specific marine wind farm in China (Wang et al., 2023b). The deformation pattern observed in this study closely resembles the measurement results. While the magnitude of the observed deformations is not identical to that of the field measurements, these findings nonetheless provide valuable insights into the applicability of pile-soil interaction models and the settlement deformation of the surrounding soil.

From a microscopic perspective, the phenomenon occurs because large-scale shear deformation causes the sand around the pile to initially expand and then contract. Before the load action, the soil around the pile was dense. When environmental loads acted, sheared soil particles within 1D range of the pile slipped past surrounding particles, increasing volume and forming a “crescent-moon shape” uplift behind the pile.

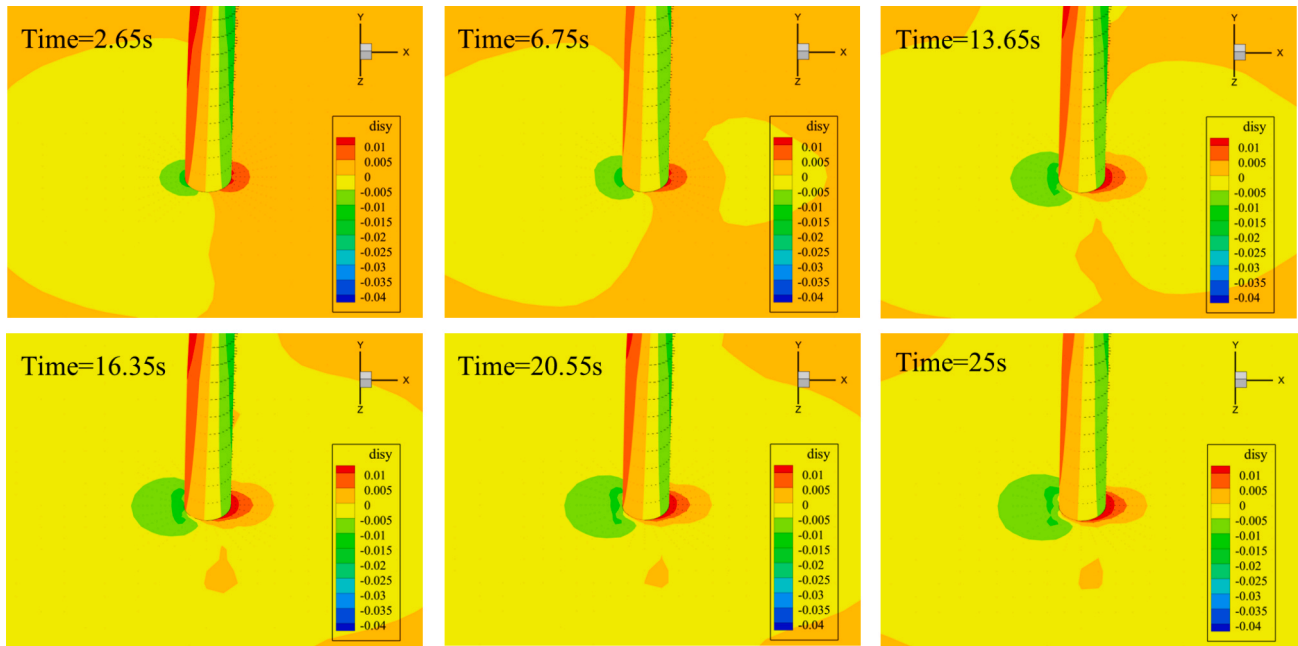


Fig. 35. Environmental load (Case 3) Cloud map of settlement development around piles.

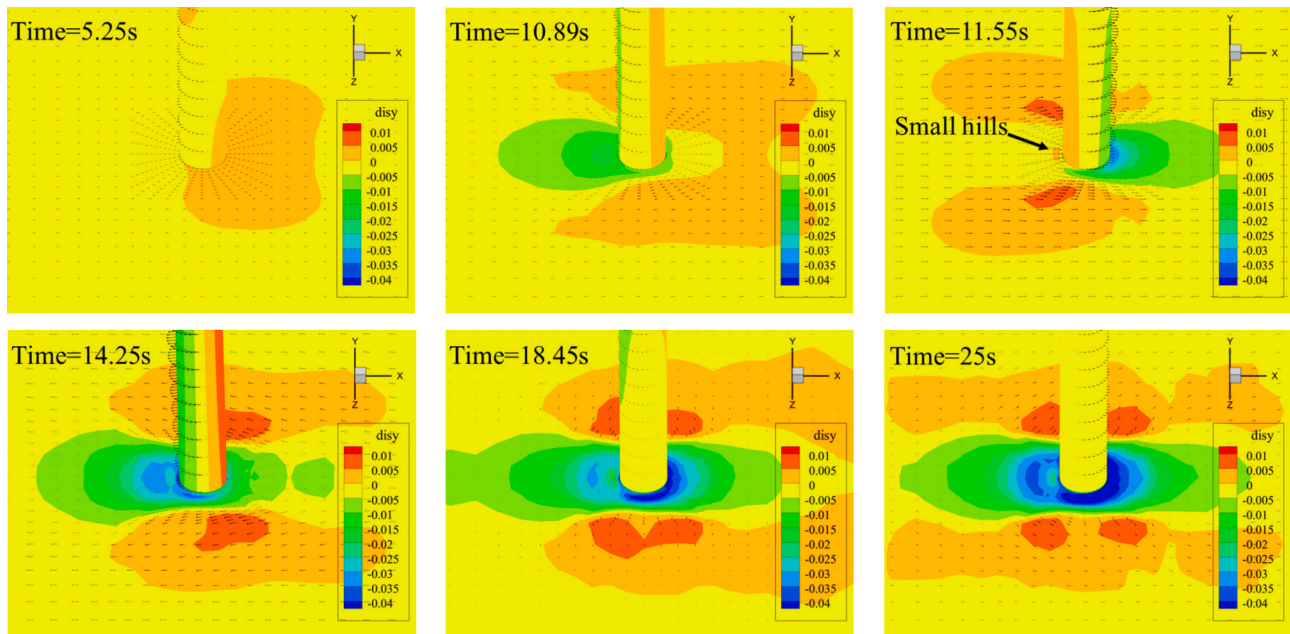


Fig. 36. Seismic load (Case 4) cloud map of settlement development around piles.

However, the upper soil around the pile consists of loose sand with a larger pore volume. After seismic loads, some sheared particles filled these pores, causing settlement within 1.5D range of the pile, more pronounced in front. As a result, both the soil in front and behind the pile experience settlement. Due to the repeated seismic shear, more and more soil particles within the 2D range behind the pile undergo dislocation and sliding, causing an increase in soil volume on both sides of the pile and resulting in slight heaving. Eventually, this causes the pile foundation to rotate. It is recommended to enhance monitoring and protection of soil displacement on the leeward side. For example, adding a riprap layer around the pile can resist scour and liquefaction responses (Mutlu Sumer et al., 2010; Escribano and Brennan, 2017), or installing geogrids around the pile can reduce liquefaction responses (Cao et al.,

2023).

4.7. The impact of the large-scale trend

Based on the above method and using the 0.2 g ChiChi earthquake wave, the dynamic responses of a typical 5 MW MOWT (NEAL) were compared. The dimensions of the MOWT model are detailed in Jonkman et al. (2009). As shown in Fig. 40, except for the case of $R_d = 0$, the permanent cumulative rotation response at the mudline for the 5 MW turbine almost exceeds 0.25° , whereas the 10 MW OWT can still meet the SLS requirements even at $R_d = 0.35$. This indicates that the increase in pile diameter and self-weight of the 10 MW OWT enhances the anti-overturning capacity of the pile foundation at the mudline.

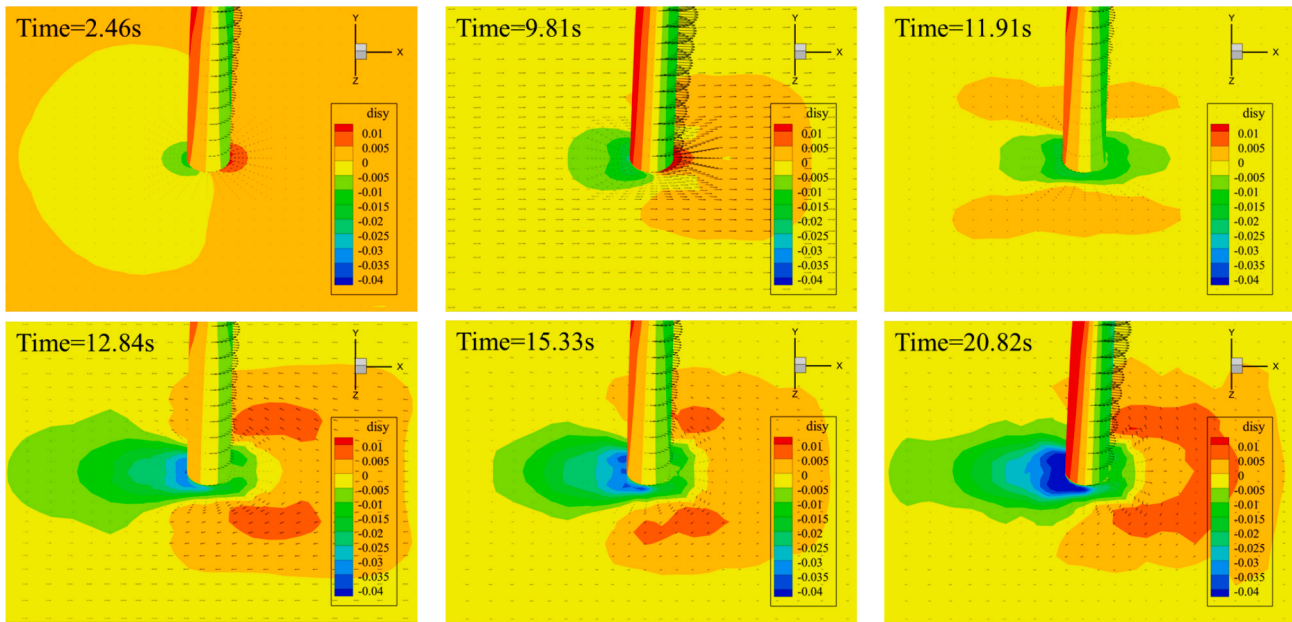


Fig. 37. Environmental and Seismic load (Case 1) cloud map of settlement development around piles.

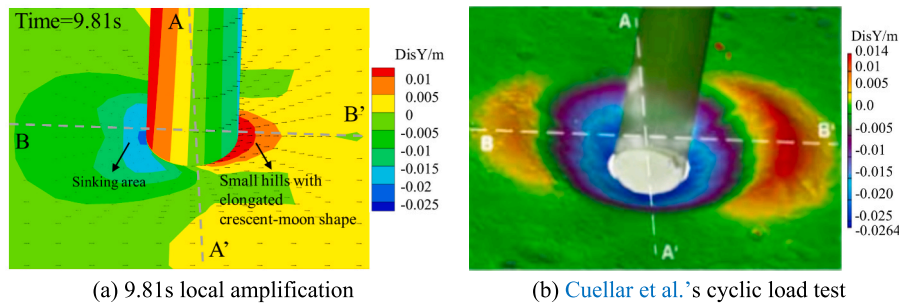


Fig. 38. Comparison of settlement around pile of liquefied seabed.

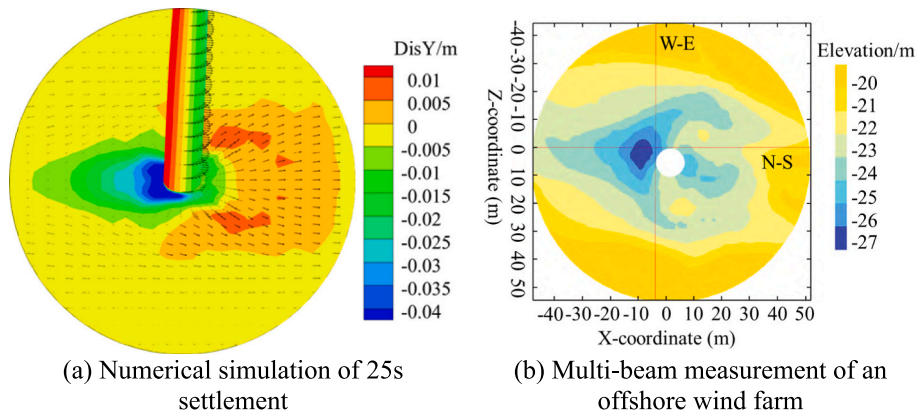


Fig. 39. Comparison of final settlement around seabed piles from numerical simulation and field measurement.

Fig. 41 compares tower-top horizontal displacements of 5 MW and 10 MW MOWTs. Excessive mudline rotation causes the 5 MW turbine to exceed the SLS, risking RNA damage, requiring deeper embedment or larger pile diameters. In contrast, the 10 MW turbine demonstrates greater structural stability and can be installed on sandy seabeds with $R_d \leq 0.35$.

Therefore, the 10 MW MOWTs not only reduces power generation costs but also enhances cost efficiency for enterprises through the

maturity of monopile technology and lower installation costs. Additionally, its inherent stability enables it to handle more complex seabed conditions. Further research on increasing turbine capacity and promoting 10 MW MOWTs is recommended.

5. Conclusions

Using the state-dependent generalized plastic constitutive model

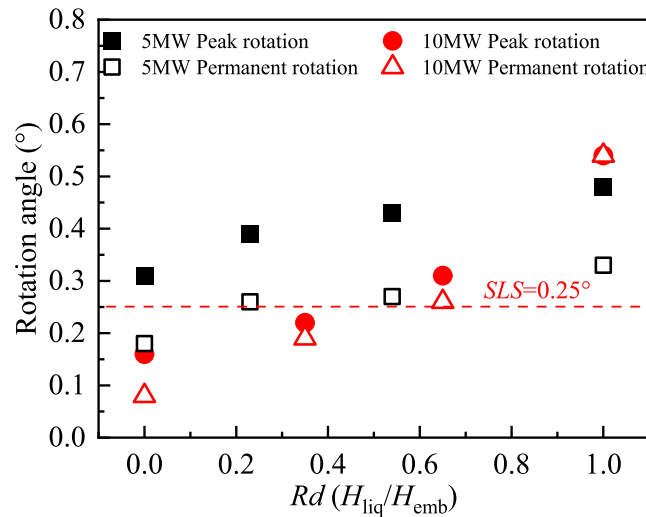


Fig. 40. Comparison of the rotation angle at the mudline between 5 MW and 10 MW MOWTs.

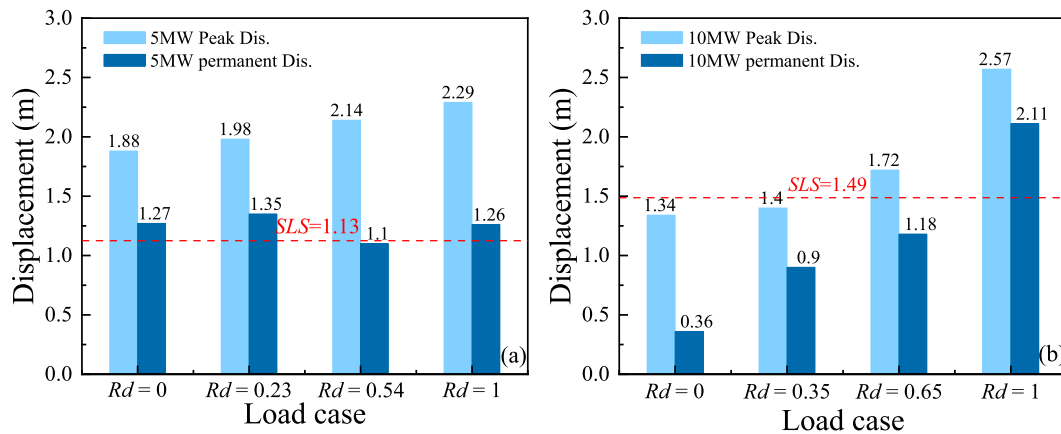


Fig. 41. Comparison of horizontal displacements at the tower top between 5 MW and 10 MW MOWTs.

(PZ-DUT) and SBFEM-FEM method for saturated porous media, we developed a cross-scale refined 3D numerical model. The study considers the influence of the relative depth (Rd) of liquefiable sand on 10 MW monopile offshore wind turbines (MOWTs). Specifically, this research examines rotation, displacement, acceleration, and the distribution of pore water pressure. The key findings are summarized as follows:

- (1) The influence of pile-soil interaction on pore pressure extends to approximately 3.2D. The pore pressure accumulation from seismic loading is more significant than that from environmental loading. The soil at the far pile (3.2D) has less vibratory pore pressure. The near pile (1D) shows obvious cyclic liquefaction.
- (2) Higher seismic intensity increases ru at the seabed and pile toe, expands the seabed liquefaction zone, and amplifies MOWTs displacement and mudline rotation. Low-intensity earthquakes exhibit a pronounced acceleration amplification effect on MOWTs, whereas this effect diminishes under high-intensity earthquakes.
- (3) The depth and range of soil liquefaction increase with Rd . When Rd exceeds 0.65, the liquefaction depth stabilizes due to increased soil confining pressure and significant seismic wave energy loss. Nonetheless, the soil at this depth exhibits a relatively weak resistance to liquefaction.

- (4) Earthquake loads affect the vibration rotation angle and peak rotation angle of the pile foundation at the mudline, while environmental loads affect the cumulative rotation angle. Environmental loads are the primary cause of accumulated rotation in MOWTs. The combined effects of environmental and earthquake loads will significantly increase the cumulative rotation angle at the mudline.
- (5) The soil strain around the pile, MOWT deflection, and rotation angle increase with Rd and decrease with sandy soil relative density. Despite ru not exceeding 0.8 for sandy soil with $Dr = 55\%$, both the pile's mudline horizontal displacement and tower top displacement exceed the limit state requirements. For this study's conditions, Rd for 10 M MOWT should be kept below 0.35.
- (6) When soil liquefaction occurs, significant settlement is observed within a range of one pile diameter (1D, where D is the pile diameter, $D = 10.375$ m) around the pile. Within a range of 2D behind the pile, the soil undergoes lateral flow and uplift, leading to rotational failure of the pile. Enhancing displacement monitoring and soil protection behind the pile is advised. Adding a riprap layer or geogrids around the pile can effectively reduce liquefaction effects.

CRediT authorship contribution statement

Tianju Wang: Writing – original draft, Visualization, Validation,

Software, Investigation. **Degao Zou:** Writing – review & editing, Supervision, Resources, Project administration, Methodology. **Jingmao Liu:** Methodology, Formal analysis, Data curation. **Kai Chen:** Visualization, Project administration, Funding acquisition. **Xiuyang Zhang:** Validation, Software. **Guoyang Yi:** Visualization, Software.

Declaration of competing interest

The authors declare that they have no known competing financial

interests or personal relationships that could have appeared to influence the work reported in this paper.

Acknowledgements

This work was supported by the National Natural Science Foundation of China (Grant Nos. 52479119 and 52192674). The authors gratefully acknowledge the financial support and express their sincerest gratitude.

Appendix A

A three-dimensional finite element model was developed using GEODYNA software (Zou et al., 2022) to simulate the aforementioned centrifuge test, as illustrated in Fig. 5. At prototype scale, the soil domain measures 46 m in length, 16 m in width, and 20.7 m in height, discretized into a mesh comprising 20,536 elements. Element sizes near the single pile were maintained below one-tenth of the wavelength corresponding to the maximum frequency of 20 Hz, following Watanabe et al. (2017). To enhance computational efficiency while preserving accuracy, a coupled SBFEM-FEM approach was employed for saturated porous media, with octree discretization techniques applied for multi-scale modeling. The transition element in this study was modeled using high-precision SBFEM (Song and Wolf, 1997; Zhang et al., 2022a,b), featuring 9 faces and 13 nodes.

The pile foundation was characterized by a Young’s modulus of 210 GPa, a density of 7800 kg/m3, and a Poisson’s ratio of 0.3. Discretization of the pile foundation and superstructure was performed using eight-node hexahedral elements, resulting in a mesh of 8256 elements. The equivalent stiffness and density method yielded an equivalent solid pile with a density of 300 kg/m3 and a Young’s modulus of 14.6 GPa.

Pile-soil interaction was modeled using zero-thickness ideal elasto-plastic interface elements (Zou et al., 2013). Zhang et al. (2024), based on Said et al. (2009), calibrated the interface parameters and successfully applied them to a large-diameter monopile foundation model in sandy soil.

Table 7
Interface parameters between steel and sand.

k_1	$k_2(\text{kPa/m})$	n	φ
800	1×10^7	0.5	27

The model’s base and sides were set as impermeable boundaries, with the top permeable. The base was fully constrained in all directions. To model X-direction seismic wave propagation, tie constraints in the Y-O-Z plane enforced equal displacements at corresponding elevations on opposite sides, avoiding wave reflection.

The soil was modeled using the generalized plasticity constitutive model (PZ-DUT) with parameters tuned to reflect sandy soil’s dynamic response. Following Wilson (1998), a damping ratio of 5 % was assumed for the soil material. The pile was modeled with a linear elastic constitutive law, and a 1 % damping ratio was assigned to the superstructure and pile foundation.

Dynamic analysis proceeded in two steps: (1) gravity was applied to the soil domain to generate the initial stress field, with zero initial displacement; (2) X-direction seismic acceleration was introduced at the base.

Data availability

Data will be made available on request.

References

Abbasi, H., Binesh, S.M., El Naggar, M.H., 2023. Response analysis of single pile embedded in saturated sand under bidirectional cyclic loading. *Soil Dyn. Earthq. Eng.* 166, 107756.
Achmus, M., Kuo, Y.S., Abdel-Rahman, K., 2009. Behavior of monopile foundations under cyclic lateral load. *Comput. Geotech.* 36 (5), 725–735.
American Petroleum Institute (API), 2011. Petroleum and Natural Gas Industries-specific Requirements for Offshore Structures. Part 4 - Geotechnical and Foundation Design Considerations. American Petroleum Institute, Washington.
Arulmoli, K., Muraleetharan, K., Hossain, M., Fruth, L., 1992. VELACS (Verification of Liquefaction Analyses by Centrifuge Studies) Laboratory Testing Program: Soil Data Report.
Asareh, M.A., Prowell, I., 2011. Seismic Loading for FAST. No. NREL/SR-5000-53872. National Renewable Energy Laboratory, Golden, CO.
Asareh, M.A., Prowell, I., Volz, J., Schonberg, W., 2016. A computational platform for considering the effects of aerodynamic and seismic load combination for utility scale horizontal axis wind turbines. *Earthq. Eng. Eng. Vib.* 15 (1), 91–102.
Bardet, J.-P., 1996. Scaled Memory Description of Hysteretic Material Behavior. *J. Appl. Fluid. Mech.* 63.
Beatty, M.H., Byrne, P.M., 2011. UBSCAND constitutive model version 904aR 2011; Itasca UDM Web Site, 69 (3).
Binh, L., Ishihara, T., Phuc, P., Fujino, Y., 2008. A peak factor for non-Gaussian response analysis of wind turbine tower. *J. Wind Eng. Ind. Aerodyn.* 96, 2217–2227.

Boulanger, R., Ziotopoulou, K., 2015. PM4Sand (Version 3): a sand plasticity model for earthquake engineering applications. Report No. UCD/CGM-15/01. Davis, CA: Center for Geotechnical Modeling, University of California.
Brandenberg Scott, J., Zhao, M., Boulanger Ross, W., Wilson Daniel, W., 2013. p-y Plasticity Model for Nonlinear Dynamic Analysis of Piles in Liquefiable Soil. *J. Geotech. Geoenviron. Eng.* 139 (8), 1262–1274.
Byrne, B., Leblanc, C., Houlsby, G., 2010. Response of stiff piles to long term cyclic loading. *Geotechnique* 60, 79–90.
Cao, G.W., Chen, Z.X., Wang, C.L., Ding, X.M., 2020. Dynamic responses of offshore wind turbine considering soil nonlinearity and wind-wave load combinations. *Ocean Eng.* 217, 108155.
Cao, Y., Kurimoto, Y., Zhou, Y.-G., Ishikawa, A., Chen, Y., 2023. Centrifuge model tests on liquefaction mitigation effect of soil-cement grids under large earthquake loadings. *Bull. Earthq. Eng.* 21 (9), 4217–4236.
Chen, K., Zou, D., Kong, X., Yu, X., 2018. An efficient nonlinear octree SBFEM and its application to complicated geotechnical structures. *Comput. Geotech.* 96, 226–245.
Chen, K., Zou, D., Liu, J., Zhuo, Y., 2023. A high-precision formula for mixed-order polygon elements based on SBFEM. *Comput. Geotech.* 155, 105209.
Chen, K., Zou, D., Tang, H., Liu, J., Zhuo, Y., 2021. Scaled boundary polygon formula for cosserat continuum and its verification. *Eng. Anal. Bound. Elem.* 126, 136–150.
Cheng, X., El Naggar, M.H., Lu, D., Wang, P., Tu, W., 2022. A cyclic p-y elastoplastic model applied to lateral loaded pile in soft clays. *Can. Geotech. J.* 60 (6), 885–901.
Cheng, X., Li, Y., Mu, K., El Naggar, M.H., Zhou, Y., Wang, P., Sun, X., Liu, J., 2024. Seismic response of tripod suction bucket foundation for offshore wind turbine in sands. *Soil Dyn. Earthq. Eng.* 177, 108353.
Cheng, X., Wang, T., Zhang, J., Wang, P., Tu, W., Li, W., 2023. Dynamic response analysis of monopile offshore wind turbines to seismic and environmental loading considering the stiffness degradation of clay. *Comput. Geotech.* 155, 105210.
Cheng, X., Wang, T., Zhang, J., Liu, Z., Cheng, W., 2021. Finite element analysis of cyclic lateral responses for large diameter monopiles in clays under different loading patterns. *Comput. Geotech.* 134, 104104.

- Cuéllar, P., Georgi, S., Baeßler, M., Rücker, W., 2012a. On the quasi-static granular convective flow and sand densification around pile foundations under cyclic lateral loading. *Granul. Matter* 14 (1), 11–25.
- Cuéllar, P., Baeßler, M., Georgi, S., Rücker, W., 2012b. Pore pressure buildup and soil stress relaxation in monopile foundations of offshore wind converters. *Bautechnik* 89 (9), 585–593.
- Cui, C., Liang, Z., Xu, C., Xin, Y., Wang, B., 2023. Analytical solution for horizontal vibration of end-bearing single pile in radially heterogeneous saturated soil. *App. Math. Model.* 116, 65–83.
- Dangaard, M., Andersen, J.K.F., 2012. Natural Frequency And Damping Estimation of an Offshore Wind Turbine Structure, The Twenty-second International Offshore and Polar Engineering Conference, pp. ISOPE-I-12-126.
- Det Norske Veritas (DNV), 2013. DNV-OS-J101 Design of Offshore Wind Turbine Structures. Det Norske Veritas AS.
- Escribano, D.E., Brennan, A.J., 2017. Stability of scour protection due to earthquake-induced liquefaction: Centrifuge modelling. *Coast. Eng.* 129, 50–58.
- Eslami, A., Ghorbani, A., 2022. Seismic response of offshore wind turbines supported on Monopiles and Suction Buckets: Numerical modelling and soft computing study. *Soil Dyn. Earthq. Eng.* 159, 107284.
- Germanischer, L., 2010. Guideline for the certification of offshore wind turbines. Germanischer Lloyd, Hamburg.
- Goldwind, 2023. <https://www.goldwind.com/en/>.
- Gong, J., Zou, D., Kong, X., Liu, J., Qu, Y., 2021. An approach for simulating the interaction between soil and discontinuous structure with mixed interpolation interface. *Eng. Struct.* 237, 112035.
- GWEC., 2024. GLOBAL WIND REPORT 2024. Global Wind Energy Council.
- He, K., Ye, J., 2023. Dynamics of offshore wind turbine-seabed foundation under hydrodynamic and aerodynamic loads: A coupled numerical way. *Renew. Energy* 202, 453–469.
- Janalizadeh, A., Zahmatkesh, A., 2015. Lateral response of pile foundations in liquefiable soils. *J. Rock Mech. Geotech. Eng.* 7 (5), 532–539.
- Jonkman, J.M., Buhl Jr., M.L., 2005. FAST User's Guide. National Renewable Energy Laboratory Technical Report No. NREL/EL-500-38230.
- Ju, S., Huang, Y., 2019. Analyses of offshore wind turbine structures with soil-structure interaction under earthquakes. *Ocean Eng.* 187, 106190.
- Kim, D.H., Lee, S.G., Lee, I.K., 2014. Seismic fragility analysis of 5mw offshore wind turbine. *Renw. Energy* 65, 250–256.
- Kühn, M., 2001. Dynamics and design optimisation of offshore wind energy conversion systems.
- Lee, S., Kim, H., Lee, S., 2010. Analysis of aerodynamic characteristics on a counter-rotating wind turbine. *Curr. Appl. Phys.* 10, S339–S342.
- Li, X.S., 2002. A sand model with state-dependent dilatancy. *Geotechnique* 52 (3), 173–186.
- Li, J., Guan, D., Chiew, Y.-M., Zhang, J., Zhao, J., 2020. Temporal evolution of soil deformations around monopile foundations subjected to cyclic lateral loading. *Ocean Eng.* 217, 107893.
- Liaw, C.Y., Chopra, A.K., 1974. Dynamics of towers surrounded by water. *Earthq. Eng. Struct. Dynam.* 3 (1), 33–49.
- Liu, H., Kaynia, A., 2022. Monopile responses to monotonic and cyclic loading in undrained sand using 3D FE with SANISAND-MSu. *Water Conserv. Sci. Eng.* 15 (1), 69–77.
- Liu, J., Zou, D., Kong, X., 2014. A three-dimensional state-dependent model of soil-structure interface for monotonic and cyclic loadings. *Comput. Geotech.* 61, 166–177.
- Liu, J., Zou, D., Kong, X., 2018. Three-Dimensional Scaled Memory Model for Gravelly Soils Subject to Cyclic Loading. *J. Eng. Mech.* 144 (3), 04018001.
- Liu, J., Zou, D., Kong, X., 2020. A two-mechanism soil-structure interface model for three-dimensional cyclic loading. *Int. J. Numer. Anal. Meth. Geomech.* 44 (15), 2042–2069.
- Liu, J., Zou, D., Ning, F., Kong, X., 2023. A unified constitutive model for instantaneous elastic-plastic and time-dependent creep behaviour of gravelly soils under complex loading. *Can. Geotech. J.* 60 (11), 1613–1628.
- Liyanapathirana, D.S., Poulos, H.G., 2005. Pseudostatic Approach for Seismic Analysis of Piles in Liquefying Soil. *J. Geotech. Geoenviron. Eng.* 131 (12), 1480–1487.
- Madabhushi, G.S.P., Knappett, J.A., Haigh, S.K., 2010. Design of Pile Foundations in Liquefiable Soils. Imperial College Press.
- Massah-Fard, M., Erken, A., Erkmn, B., Ansal, A., 2024. Analysis of Offshore Wind Turbine by Considering Soil-Pile-Structure Interaction: Effect of Sea-Wave Load Duration. *J. Earthq. Eng.* 28 (12), 3291–3309.
- Mehrar, M., Harireche, O., Faramarzi, A., 2016. Evaluation of undrained failure envelopes of caisson foundations under combined loading. *Appl. Ocean Res.* 59, 129–137.
- Mo, R., Cao, R., Liu, M., Li, M., Huang, Y., 2021. Seismic fragility analysis of monopile offshore wind turbines considering ground motion directionality. *Ocean Eng.* 235, 109414.
- Musial, W., Ram, B., 2010. Large-scale Offshore Wind Power in the United States: Assessment of Opportunities and Barriers. National Renewable Energy Lab. (NREL), Golden, CO (United States).
- Mutlu Sumer, B., Diken, F.H., Fredsøe, J., 2010. Cover stones on liquefiable soil bed under waves. *Coast. Eng.* 57 (9), 864–873.
- Nie, X., Chen, K., Zou, D., Kong, X., Liu, J., Qu, Y., 2022. Slope stability analysis based on SBFEM and multistage polytree-based refinement algorithms. *Comput. Geotech.* 149, 104861.
- Nicholson, J.C., 2011. Design of wind turbine tower and foundation systems: Optimization approach. *J. Dissertations & Theses Gradworks*.
- Page, A.M., Klinkvort, R.T., Bayton, S., Zhang, Y., Jostad, H.P., 2021. A procedure for predicting the permanent rotation of monopiles in sand supporting offshore wind turbines. *Mar. Struct.* 75, 102813.
- Papadimitriou, A., Bouckovalas, G., 2002. Plasticity model for sand under small and large cyclic strains: a multiaxial formulation. *Soil Dyn. Earthq. Eng.* 22, 191–204.
- Patra, S.K., Haldar, S., 2021. Seismic response of monopile supported offshore wind turbine in liquefiable soil. *Structures* 31, 248–265.
- Patra, S.K., Haldar, S., Bhattacharya, S., 2022. Predicting tilting of monopile supported wind turbines during seismic liquefaction. *Ocean Eng.* 252, 111145.
- Prowell, I., Elgamal, A., Jonkman, J., FAST Simulation of Wind Turbine Seismic Response, National Renewable Energy Laboratory, Golden, Colorado, USA, 2010. Technical Report No. NREL/CP-500-46225.
- Qu, Y., Zou, D., Chen, K., Liu, J., 2021. Three-dimensional refined analysis of seismic cracking and anti-seismic measures performance of concrete face slab in CFRDs. *Comput. Geotech.* 139, 104376.
- Sahraeian, S.M.S., Masoumi, M.A., Najafgholipour, M.A., Shafiee, A., Pandey, B., 2023. Seismic response of monopile foundation of offshore wind turbines under near-field and far-field ground motions. *Soil Dyn. Earthq. Eng.* 174, 108166.
- Said, I.D., De Gennaro, V., Frank, R., 2009. Axisymmetric finite element analysis of pile loading tests. *Comput. Geotech.* 36 (1–2), 6–19.
- Santangelo, F., Failla, G., Santini, A., Arena, F., 2016. Time-domain uncoupled analyses for seismic assessment of land-based wind turbines. *Eng. Struct.* 123, 275e299.
- Sapountzakis, E.J., Dikaros, I.C., Kampitsis, A.E., Koroneou, A.D., 2015. Nonlinear response of wind turbines under wind and seismic excitations with soil-structure interaction. *J. Comput. Nonlinear Dynam.* 10 (4), 41001–41007.
- Shahir, H., Pak, A., Taiebat, M., Jeremić, B., 2012. Evaluation of variation of permeability in liquefiable soil under earthquake loading. *Comput. Geotech.* 40, 74–88.
- Shi, S., Zhai, E., Xu, C., Iqbal, K., Sun, Y., Wang, S., 2022. Influence of Pile-Soil Interaction on Dynamic Properties and Response of Offshore Wind Turbine with Monopile Foundation in Sand Site. *Appl. Ocean Res.* 126, 103279.
- Song, C., Wolf, J.P., 1997. The scaled boundary finite-element method—alias consistent infinitesimal finite-element cell method—for elastodynamics. *Comput. Methods Appl. Mech. Eng.* 147, 329–355.
- Sun, Y., Xu, C., Cui, C., Naggari, M.H.E., Du, X., 2022. Seismic Response of Monopile-Supported OWT Structure Considering Effect of Long-Term Cyclic Loading. *Int. J. Struct. Stab. Dyn.* 23 (09), 2350099.
- Teng, X. W., Research on the Analysis Method of Saturated Soil Based on Scaled Boundary Finite Element Method. PhD Thesis. Dalian, CHN: Dalian University of Technology. (In Chinese).
- Tran, M.N., 2005. Installation of suction caissons in dense sand and the influence of tilt and cemented layers. The University of Sydney, Sydney. PhD Thesis.
- Versteijlen, W.G., Metrikine, A., Hoving, J., Smidt, E., De Vries, W., 2011. Estimation of the vibration decrement of an offshore wind turbine support structure caused by its interaction with soil. In: *Proceedings of the EWEE Offshore 2011 Conference*, Amsterdam, The Netherlands, 29 November–1 December 2011. European Wind Energy Association.
- Vestas, 2022. <https://www.vestas.com/en/media/company-news>.
- Wilson, D.J., 1998. Soil-pile-superstructure interaction in liquefying sand and soft clay. University of California, Davis, USA. PhD Thesis.
- Wang, B., Cui, C., Xu, C., Meng, K., Li, J., Xu, L., 2024. A novel analytical solution for horizontal vibration of partially embedded offshore piles considering the distribution effect of wave loads. *Ocean Eng.* 307, 118179.
- Wang, P., Zhao, M., Du, X., et al., 2018. Wind, wave and earthquake responses of offshore wind turbine on monopile foundation in clay. *Soil Dyn. Earthq. Eng.* 113, 47–57.
- Wang, R., Fu, P., Zhang, J.-M., 2016. Finite element model for piles in liquefiable ground. *Comput. Geotech.* 72, 1–14.
- Wang, X., Wang, W., Li, J., 2023a. Assessment on earthquake-induced liquefaction around a hybrid monopile foundation for offshore wind turbines with a transition layer model. *Ocean Eng.* 282, 115028.
- Wang, Z., Huan, C., Chen, L., 2023b. Research of Real-time Monitoring for Local Scour of Offshore Wind Power Pile Foundation Based on Sonar Image. *J. Ocean Technol.* 42 (04), 91–99. In Chinese.
- Wang, Z.L., Dafalias Yannis, F., Shen, C.K., 1990. Bounding Surface Hypoplasticity Model for Sand. *J. Eng. Mech.* 116 (5), 983–1001.
- Watanabe, K., Pisan'o, F., Jeremić, B., 2017. Discretization effects in the finite element simulation of seismic waves in elastic and elastic-plastic media. *Eng. Comput.-Germany* 33 (3), 519–545.
- Wu, X., Hu, Y., Li, Y., et al., 2019. Foundations of offshore wind turbines: A review. *J. Renew. Sustain. Energy Rev.* 104, 379–393.
- Xi, R., Wang, P., Du, X., Xu, C., 2021. Dynamic behaviors of wind turbines under wind and earthquake excitations. *J. Renew. Sustain. Energy Rev.* 13 (4), 043306.
- Yan, Y., Li, C., Li, Z., 2021. Buckling analysis of a 10 MW offshore wind turbine subjected to wind-wave-earthquake loadings. *Ocean Eng.* 236, 109452.
- Yang, Y., Bashir, M., Li, C., Michailides, C., Wang, J., 2020. Mitigation of coupled wind-wave-earthquake responses of a 10 MW fixed-bottom offshore wind turbine. *Renew. Energy* 157, 1171–1184.
- Zhang, J., Yuan, G.-K., Zhu, S., Gu, Q., Ke, S., Lin, J., 2022a. Seismic Analysis of 10 MW Offshore Wind Turbine with Large-Diameter Monopile in Consideration of Seabed Liquefaction. *Energies* 15 (7), 2539.
- Zhang, J., Zhao, M., Eisenträger, S., Du, X., Song, C., 2022b. An asynchronous parallel explicit solver based on scaled boundary finite element method using octree meshes. *Comput. Methods Appl. Mech. Eng.* 401, 115653.

- Zhang, X., Zou, D., Liu, J., Chen, K., Li, X., Wang, T., 2024. A developed soil reaction model for large- diameter monopiles in sand based on hyperbolic curves. *Comput. Geotech.* 172, 106468.
- Zhang, X., Zou, D., Liu, J., Chen, K., Ning, F., Wang, T., 2025. A unified soil reaction model for laterally loaded monopiles in soft and stiff clays. *Comput. Geotech.* 177, 106819.
- Zhao, X., Maisser, P., 2006. Seismic response analysis of wind turbine towers including soil-structure interaction. *J. Proceedings of the Institution of Mechanical Engineers Part K Journal of Multi-body Dynamics.* 220(1):53-61.
- Zou, D., Kong, X., Liu, J., et al., 2022. Theoretical Introduction and User Manual of the GEODYNA7.0 : A High-Performance Finite Element Analysis Software System for Large-Scale Geotechnical Engineering. Dalian University of Technology, Dalian.
- Zou, D., Teng, X., Chen, K., Liu, J., 2019. A polyhedral scaled boundary finite element method for three-dimensional dynamic analysis of saturated porous media. *Eng. Anal. Bound. Elem.* 101, 343–359.
- Zou, D., Xu, B., Kong, X., Liu, H., Zhou, Y., 2013. Numerical simulation of the seismic response of the Zipingpu concrete face rockfill dam during the Wenchuan earthquake based on a generalized plasticity model. *Comput. Geotech.* 49, 111–122.
- Zuo, H., Bi, K., Hao, H., 2018. Dynamic analyses of operating offshore wind turbines including soil-structure interaction. *Eng. Struct.* 157, 42–62.